Journal of Geophysical Research: Solid Earth

RESEARCH ARTICLE
10.1029/2018JB015961

An Improved Method to Determine Coda-Q, Earthquake Magnitude, and Site Amplification: Theory and Application to Southern California

W. Wang[1] and P. M. Shearer[1]

[1] Institute of Geophysics and Planetary Physics, Scripps Institution of Oceanography, University of California, San Diego, La Jolla, CA, USA

Key Points:
- We develop a new coda-Q method to determine coda magnitudes, site amplification factors, and coda attenuation simultaneously
- We introduce a sourceside coda attenuation together with the conventional stationside coda attenuation considering complex attenuation
- The multiple frequency source terms can be used to study the source spectral models and earthquake scaling relation

Supporting Information:
- Supporting Information S1

Correspondence to:
W. Wang,
weiwang053@gmail.com

Citation:
Wang, W., & Shearer, P. M. (2019). An improved method to determine coda-Q, earthquake magnitude, and site amplification: Theory and application to southern California. *Journal of Geophysical Research: Solid Earth*, *124*, 578–598. https://doi.org/10.1029/2018JB015961

Received 13 APR 2018
Accepted 30 NOV 2018
Accepted article online 3 DEC 2018
Published online 12 JAN 2019

Abstract Seismic coda waves can be used to constrain attenuation, estimate earthquake magnitudes, and determine site amplification factors. We have developed a new multistation and multievent method to determine these three important seismic parameters simultaneously. We analyze 642 representative local (≤100 km) and shallow (≤20 km) earthquakes with catalog magnitudes between 1.8 and 5.4 in southern California at multiple frequency bands centered at 1.5, 3, 6, and 12 Hz. We find that the length of the moving average time window can affect the measurement of coda attenuation Q_C, but our tests indicate that the optimal window length is about 15 times the dominant data period. We use linear regression to fit each coda section and use only those portions that agree with the model decay rate with a correlation coefficient larger than 0.9. For a frequency-dependent coda-Q_C model ($Q_C = Q_0 f^n$) at 1-Hz reference frequency, our results yield estimates for Q_0 and n of 107–288 and 0.42–1.14, respectively. Our coda magnitude estimates are linearly correlated with catalog magnitudes, and our observed lateral variations in coda-Q_C and our site amplification factors are in general agreement with previous results, although there are notable differences at some locations. This approach provides a unified, accurate, and stable method to measure coda-Q_C, earthquake magnitude, and site amplification using coda waves of locally recorded earthquakes.

1. Introduction

Since Aki (1969) and Aki and Chouet (1975) first interpreted coda waves using a single-scattering model, many methods have been developed to relate seismic attenuation to coda wave properties. Attenuation is characterized by the quality factor Q, whose reciprocal is the fractional energy loss per cycle of the passing wave. The coda energy decay can be expressed as

$$E(f,t) = S(f)R(f)t^{-\alpha}e^{-2\pi ft/Q_C(f)} \quad (1)$$

where E is the power spectrum, S is a frequency-dependent source amplitude term, R is a frequency-dependent station amplitude term, t is the lapse time, f is the frequency, α is a positive constant that is related to geometrical spreading and wave type (Aki & Chouet, 1975), and Q_C is the coda quality factor. Some studies indicate that the value of coda attenuation, Q_C^{-1}, correlates with tectonics. High Q_C^{-1} values are observed in active regions and low values in stable regions (e.g., Hiramatsu et al., 2000; Hoshiba, 1993; Jin & Aki, 2005; Mitchell et al., 1997; Sato et al., 2012; Singh & Herrmann, 1983).

The properties of Q_C are of great interest. Rautian and Khalturin (1978) first observed that the measured Q_C depends on the lapse time, and ensuing studies reported an increase of Q_C with lapse time all around the world (e.g., Calvet & Margerin, 2013; Carcolé & Sato, 2010; Hiramatsu et al., 2000; Ibanez et al., 1990; Mukhopadhyay et al., 2008; Phillips & Aki, 1986; Yoshimoto & Jin, 2008). Another research question is whether there are temporal changes in Q_C associated with seismicity. Some studies found evidence that coda attenuation Q_C may change prior to earthquakes (e.g. Jin & Aki, 1988; Su & Aki, 1990), and others observed a change of Q_C just before or after the earthquakes (e.g., Huang & Kisslinger, 1992; Peng et al., 1987; Tsukuda, 1988; Wang et al., 1989). However, other studies, including several that used similar earthquake pairs, have not obtained clear temporal changes in coda Q_C (e.g., Aster et al., 1996; Beroza et al., 1995; Hellweg et al., 1995; Huang & Wyss, 1988; Sumiejski & Shearer, 2012; Tselentis, 1997; Woodgold, 1994).

The physical meaning of coda-Q has also been widely discussed. Several studies have shown that coda waves are predominantly composed of scattered S waves (Aki & Chouet, 1975; Kato et al., 1995; Tsujiura, 1978). Coda attenuation contains contributions from both scattering attenuation and intrinsic attenuation, and separating these two factors is a long-standing problem in seismology. There are two end-member models used to interpret coda attenuation, the single-scattering model and the diffusion model. The single-scattering model predicts that coda attenuation is a combination of scattering and intrinsic attenuation, $Q_C^{-1} = Q_{Sc}^{-1} + Q_I^{-1}$, while the diffusion model shows that Q_C asymptotically approaches the intrinsic attenuation Q_I at increasing times in the coda wave train in a simple uniform half-space (Shapiro et al., 2000). Other studies (Margerin et al., 1998, 1999; Wegler, 2004; Yomogida et al., 1997) use more complex but more realistic layer model to study the Q_C and indicate that the relation between Q_C and intrinsic and scattering attenuation structure is complicated. Margerin et al. (1998) first pointed out the "leakage effect," which significantly affects Q_C in the layered models in the low-frequency range.

Determining the sensitivity of coda-Q in both scattering and intrinsic attenuation is an area of active research (Margerin et al., 1998, 1999; Wennerberg, 1993), in which advanced simulation methods such as radiative transfer are applied to more realistic depth-dependent models than the simple models that motivated early coda research (Wang & Shearer, 2017). We do not address these issues here, as we adopt an empirical approach to examine the origin of coda-Q variations in southern California, without attempting to resolve specific physical models that can explain coda-Q and its variations. We hope, however, that improved observational constraints on coda-Q will inform future modeling by identifying interesting signals to be explained, in particular, the scale length of coda-Q variations and whether they are more coherent when mapped to station or source locations.

Earthquake magnitude is an important parameter for a variety of investigations. Current methods to determine magnitude depend on the amplitude of body waves, or on coda duration and/or amplitude (e.g., Archuleta et al., 1982; Bakun, 1984; Denieul et al., 2015; Eaton, 1992; Hawthorne et al., 2017; Herrmann, 1975; Lee et al., 1972; Mayeda et al., 2003; Sens-Schönfelder & Wegler, 2006). However, estimated magnitudes from body wave amplitudes can be biased by the source radiation pattern and raypath focusing and defocusing anomalies (Mayeda et al., 2003). Since coda wave magnitudes were first implemented by Johnson (1979) and Suteau and Whitcomb (1979), coda wave magnitudes have proven to be more stable compared to other methods (Mayeda & Walter, 1996; Mayeda et al., 2003), as scattering tends to average out much of the spatial variability seen in direct-wave amplitudes.

Understanding and measuring site amplification is a fundamental problem for seismologists and earthquake engineers and helps to improve strong ground motion estimates. Since the late coda is dominantly shear waves, the site amplification of coda waves closely approximates that of direct shear waves (Kato et al., 1995; Phillips & Aki, 1986; Tsujiura, 1978). By comparing results from direct shear waves and coda waves, Tsujiura (1978) and Tucker and King (1984) argued that coda waves provide a more stable estimate of site effects, because the coda waves are composed of scattered seismic waves from different directions and average the heterogeneities around the source and receiver.

Based on a variety of research goals, previous studies have developed different methods to measure coda-Q, source amplitude terms (e.g., magnitude), and site terms (e.g. Boatwright et al., 1991; Eulenfeld & Wegler, 2016; Mayeda & Walter, 1996; Prieto et al., 2004; Shearer et al., 2006). Starting with equation (1), most studies have attempted to separate the three terms, eliminate two of them, and solve for the remaining term of interest (i.e., most coda-Q studies remove the source and station terms and then use linear regression to fit the coda energy decay). Dewberry and Crosson (1995) focus on the earthquake source by first fitting for coda-Q from individual records and then using least squares inversion to solve for the best fitting source and station amplitude terms, assuming the single-scattering model. Mayeda and Walter (1996) used an empirical raypath correction based on 2-D multiple scattering to estimate the coda magnitude and spectra. Later, Eulenfeld and Wegler (2016) developed an improved method to fit the envelopes of direct S wave and S coda to resolve source amplitude terms and site terms, together with attenuation terms (intrinsic and scattering attenuation), and applied this method to data from USarray (Eulenfeld & Wegler, 2017). They used an analytic approximate solution of 3-D isotropic radiative transfer theory (Paasschens, 1997) to model the scattering effect to separate intrinsic and scattering attenuation.

Southern California is one of the most well-studied seismically active regions in the world and has seen a variety of studies on seismic attenuation structure (Aki, 1996; Frankel et al., 1990; Hauksson & Shearer, 2006;

Lin & Jordan, 2018; Mayeda, Koyanagi, & Aki, 1991; Mayeda, Su, & Aki, 1991; Raoof et al., 1999; Wang & Shearer, 2017) and source properties and site effects (Ben-Zion & Zhu, 2002; Boatwright et al., 1991; Kato et al., 1995; Prieto et al., 2004; Shearer et al., 2006; Su & Aki, 1995; Trugman & Shearer, 2017). Here based on equation (1), we invert the data to resolve simultaneously the coda attenuation Q_C, the source amplitude terms, and the station amplitude terms, assuming the multiple-scattering model from late *S* coda (>2 times *S* travel time). To reduce the size of the inverse problem, we show how to set up a simplified problem with much fewer time points than the original data, but which produces the same L2-norm solution. To consider lateral variations in the attenuation structure in southern California, we introduce a sourceside attenuation term together with the conventional station attenuation term to describe the coda energy decay. We show how our source amplitude term estimates can be related to coda magnitude and compare our coda attenuation and site amplification terms to those obtained in previous studies.

2. Data Selection and Proceeding

2.1. Data Selection

We select local events from a relocated catalog (Yang et al., 2012) from 2000 to 2013 and download waveform data using the Seismogram Transfer Program (STP) available from the Southern California Earthquake Center (SCEC). We use only events shallower than 20 km and stations at less than 100 km epicentral distance (to focus on body waves) (see Figure 1). We require three components (either short-period (EH) or broadband (HH, BH) seismometers), since we compute the smoothed energy densities based on vector summation of the three components. The seismograms are generally sampled at 100 Hz.

Most coda-*Q* studies have examined station-averaged coda-*Q*, requiring a minimum number of recorded events at each station to obtain stable estimates. For our multistation and multievent method (MSMEM), we also require both a minimum number of stations recording each event and events recorded by each station, and have found that a threshold of 20 events per station and 20 stations per event is enough to yield stable results. We filter the seismograms with a fourth-order zero-phase Butterworth filter at the following octave frequency bands: 1–2, 2–4, 4–8, and 8–16 Hz. For each trace, we estimate the noise level by using the energy densities in a 3-s time window before the *P* wave arrival and the coda level from a 40-s window starting at the 50-s lapse time used to measure the coda attenuation at each frequency band. We require that the coda level be at least 5 times larger than the preevent noise level.

3. Methodology: Multiple Station and Multiple Event Method

3.1. Single Station and Multiple Event Method

Even if the dependence of measured coda attenuation Q_C on the components is weak, the site amplifications between vertical and horizontal components may be different (Kato et al., 1995). We directly measure coda attenuation Q_C from the energy densities. We rewrite equation (1) as

$$E_{ij}(f,t_k) = S_i(f)R_j(f)t_k^{-\alpha}e^{-2\pi f t_k/Q_{Cij}}, \tag{2}$$

where E_{ij} indicates the energy density of the coda wave, S_i indicates the *i*th source amplitude term, R_j indicates the *j*th station amplitude term, and Q_{Cij} is the quality factor of the coda wave for the raypath between the *i*th source and *j*th station. To implement linear inversion, we take the natural logarithm and obtain

$$e_{ij}(f,t_k) = s_i(f) + r_j(f) + (-\alpha)\log(t_k) + \frac{-2\pi f}{Q_{Cij}(f)}t_k \tag{3}$$

where e_{ij}, s_i, and r_j denote $\log E_{ij}$, $\log S_i$, and $\log R_j$, respectively.

Conventional methods measure the coda attenuation Q_C from the waveforms by only considering the time-dependent terms in equation (3). Assuming the geometrical spreading term α is a constant, for example, α is set to 2 for body wave coda studies, assuming the single-scattering model (Aki & Chouet, 1975; Carcolé & Sato, 2010; Dewberry & Crosson, 1995). In this study, we use $\alpha = 1.5$ estimated from 3-D diffusion theory in a whole space (Margerin et al., 1998; Paasschens, 1997). We find that the choice of α does not effect the results significantly (see section 5). We can express (3) as

$$b_{ij}(f,t_k) = e_{ij}(f,t_k) + \alpha\log(t_k) = C_{ij} + \frac{-2\pi f}{Q_{Cij}(f)}t_k \tag{4}$$

in which we subtract $-\alpha \log(t_k)$ from our original coda power time series, $a(t)$, to create a new time series, $b(t)$, which has been corrected for geometrical spreading. For each $b(t)$, we can apply simple linear regression to solve for the best fitting amplitude factor C and slope parameter $-2\pi f/Q_C$. This provides a separate coda attenuation estimate Q_C^{-1} for each seismogram. Assuming that much of the variation Q_C^{-1} is caused by near-station differences, the values Q_C^{-1} obtained at each station can be averaged to obtain a measure of the average attenuation properties around the station (Aki, 1996; Carcolé & Sato, 2010; Jin & Aki, 1988). We term this commonly applied approach the Single Station and Multiple Event Method (SSMEM). Notice that by replacing the separate event and station amplitude factors s_i and r_j in equation (3) with a seismogram-specific scaling factor, C_{ij}, the model now has many more free parameters.

Previous studies have shown that the coda attenuation Q_C increases with lapse time but eventually settles at a stable value (i.e., Calvet & Margerin, 2013; Carcolé & Sato, 2010; Phillips & Aki, 1986; Rautian & Khalturin, 1978; Yoshimoto & Jin, 2008). However, the required lapse time for convergence is hard to determine precisely. It depends on a variety of factors, such as the frequency band and source location. There are two main approaches to setting the minimum lapse time for data analysis. One is to use the lapse time $\alpha r/v$, where α is a time lapse coefficient, always set to 2 (Calvet & Margerin, 2013; Carcolé & Sato, 2010; Hiramatsu et al., 2000), r is the epicentral distance, and v is the average crustal shear wave velocity. The coda waves after twice the shear wave travel time are considered independent of the source mechanisms and affected only by the multiple-scattering behavior. Another strategy is to use a constant lapse time, but long enough to ensure that the coda waves suffer enough scattering during the propagation (Calvet & Margerin, 2013; Kato et al., 1995). A further complication is that the coda attenuation measurement also depends on the length of the time window. Given the scatter in real data, a too-short window cannot reliably determine the coda decay rate, but a too-long window may extend into the low signal-to-noise regime where the coda begins to merge back into the background noise. Here we use a 40-s-long time window starting at a lapse time of 50 s. Note that 50 s is slightly more than twice the S wave travel time at the maximum epicentral distance of 100 km and that our signal-to-noise selection criteria should ensure that we are still resolving coda power at 90 s.

The squared seismograms are smoothed with a moving-average window. The length of the appropriate moving window depends on the frequency band (Calvet & Margerin, 2013; Carcolé & Sato, 2010; Phillips & Aki, 1986). The choice of averaging length can affect the measurement of coda attenuation Q_C. Most previous studies define the length as a function of the central frequency of the frequency band, $T_W = a/f$, where f is the central frequency and a is an adjustable parameter. If a is too large, the coda decay rate will change because of oversmoothing; on the other hand, if a is too small, near-zero values may persist in the coda window, which will bias the fits in the log domain. In this study, a is assigned 15, comparable to Phillips and Aki (1986) and Calvet and Margerin (2013). We use linear regression to fit each smoothed coda wave, and only those portions that agree with the model decay rate with a correlation coefficient larger than 0.9 are used for later analyses. The coda waves with positive coefficients (i.e., their amplitudes grow with time and $Q_{Cij} < 0$) are discarded. This procedure serves to remove observations contaminated by aftershocks, noise spikes, or other effects.

3.2. Multiple Station and Multiple Event Method

Because our goal is to solve for both source amplitude terms and station amplitude terms together with coda attenuation, we model C_{ij} in equation (4) as a sum of a source amplitude term s_i and station amplitude term r_j. For one coda record at frequency f we have

$$\begin{bmatrix} b_{ij}(t_1) \\ b_{ij}(t_2) \\ \vdots \\ b_{ij}(t_k) \end{bmatrix} = \begin{bmatrix} e_{ij}(t_1) \\ e_{ij}(t_2) \\ \vdots \\ e_{ij}(t_k) \end{bmatrix} + \begin{bmatrix} \log(t_1) \\ \log(t_2) \\ \vdots \\ \log(t_k) \end{bmatrix} \alpha = \begin{bmatrix} 1 \\ 1 \\ \vdots \\ 1 \end{bmatrix} s_i + \begin{bmatrix} 1 \\ 1 \\ \vdots \\ 1 \end{bmatrix} r_j + \begin{bmatrix} t_1 \\ t_2 \\ \vdots \\ t_k \end{bmatrix} \frac{-2\pi f}{Q_{Cij}} \tag{5}$$

The decay rate depends only on the average medium properties of the crust sampled by the coda waves. These properties of coda waves offer an alternative approach for studying the source and site effects on high-frequency seismic waves. Local coda waves are likely backscattered S waves from heterogeneities distributed in a volume surrounding the source and receiver (Aki, 1980; Mayeda, Koyanagi, & Aki, 1991; Koyanagi et al., 1992; Tsujiura, 1978). This explains why local S wave coda records decay at a similar rate for all source-station pairs within a localized region. However, our study region in southern California is large enough

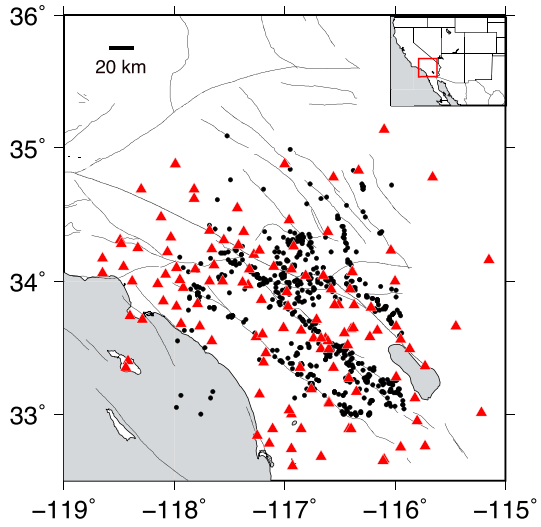

Figure 1. Locations of earthquakes and stations used in this study. The event epicenters are shown as black dots and the station locations are shown as red triangles. Quaternary faults are depicted as light black curves. The red box in the top right plot indicates our study region in the western U.S. map.

that lateral variations in attenuation structure are apparent, so modeling coda decay variations only as a function of the station location, as in the SSMEM method, may be insufficient. Because the coda decay rates at a single station can vary (see Figure 2) at all frequency ranges, we introduce another attenuation term, the sourceside attenuation term. Equation (5) is rewritten as

$$\begin{bmatrix} b_{ij}(t_1) \\ b_{ij}(t_2) \\ \vdots \\ b_{ij}(t_k) \end{bmatrix} = \begin{bmatrix} 1 \\ 1 \\ \vdots \\ 1 \end{bmatrix} s_i + \begin{bmatrix} 1 \\ 1 \\ \vdots \\ 1 \end{bmatrix} r_j + \begin{bmatrix} t_1 \\ t_2 \\ \vdots \\ t_k \end{bmatrix} \frac{-2\pi f}{Q^S_{Ci}} + \begin{bmatrix} t_1 \\ t_2 \\ \vdots \\ t_k \end{bmatrix} \frac{-2\pi f}{Q^R_{Cj}}, \tag{6}$$

where Q^S_{Ci} is the ith sourceside coda attenuation and Q^R_{Cj} is jth stationside coda attenuation. We combine the records from different stations and different events and rearrange equation (6) as **d=Gm**. The **G** matrix is large and sparse, but in principle solvable using sparse-matrix least squares methods. However, each data vector $b_{ij}(t_k)$ contains a 40-s waveform (i.e., 4,000 discrete time points), which when combined with many different events and stations, results in a very large inverse problem. To reduce the size of the problem, we define a corrected data vector $\hat{b}_{ij}(t_k) = \hat{e}_{ij}(t_k) + \alpha \log(t_k)$, where $\hat{e}_{ij}(t_k)$ is the best fitting $e_{ij}(t_k)$ by using equation (4). In the appendix, we prove that the new inverse problem has the same L2-norm solution as equation (6). Since the fit to the data vector is controlled by only two parameters, we can greatly reduce the size of the corrected data vector. In this study, we use just two points to represent each waveform instead of 4,000 points.

3.3. Error Estimation

Based on the least squares solution, the misfit function is defined as,

$$err = \frac{\sqrt{\sum_{i,j,k}(\hat{b}_{ij}(t_k) - s_i - r_j + 2\pi f t_k/Q^S_{Ci} + 2\pi f t_k/Q^R_{Cj})^2}}{\sqrt{\sum_{i,j,k}\hat{b}^2_{ij}(t_k)}}. \tag{7}$$

where i is the index for the source, j for the station, and k for the time series. The least squares method finds the parameters that minimize err. However, to avoid biasing the solution with anomalous data (outliers), we exclude some of the data as follows. We define a reference misfit based on equation (4) as

$$err^{ij}_1 = \sqrt{\sum_{k=1}^{n}(\hat{b}_{ij}(t_k) - C_{ij} - \frac{-2\pi f}{Q_{Cij}(f)}t_k)^2}. \tag{8}$$

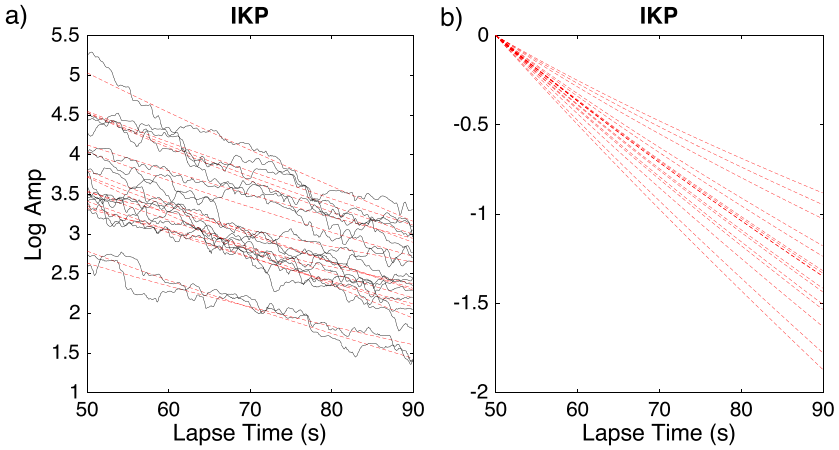

Figure 2. Observed coda energy decay curves at station IKP for different earthquakes at 2–4 Hz. Panel (a) shows mean-squared coda amplitudes (black lines) and the best-fitting curves (red dashed lines) using equation (5). Panel (b) shows the difference of the slopes of the best-fitting energy decay curves.

err_1 describes the misfit between a single coda waveform and its best fitting curve from a model that includes a custom amplitude scaling term, C_{ij}. After solving the inverse problem of equation (6), we define the new misfit for each trace as

$$err_2^{ij} = \sqrt{\sum_{k=1}^{n} (\hat{b}_{ij}(t_k) - s_i - r_j + \frac{2\pi f}{Q_{Cij}(f)} t_k)^2}. \quad (9)$$

err_2 describes the misfit between a single coda waveform and its best fitting curve from a model in which the amplitude scaling is given by the sum of a source term, s_i, and a receiver term, r_j. For some waveforms, the coda amplitude is poorly approximated by this sum and the misfit will be correspondingly larger. If $err_2 > 5 \times err_1$, we flag this trace as an outlier and remove it from the data set. After removing all the outliers, we repeat solving the inverse problem and continue removing outliers until there are no more outliers found. In this study, this process converges after four to six iterations and removes about 20% of the original data. This fraction exceeds the percentage of individual seismograms that fail the misfit test, because removal of traces will sometimes cause entire events or stations to be removed from the data set if they no longer meet the 20 stations per event and 20 events per station criteria.

The model uncertainty of the least squares inverse problem can be estimated by using the method in Menke (2012). If we assume the data are uncorrelated and the variance of the observed data is σ_d, the covariance matrix of the least squares solution m can be estimated from

$$\mathrm{cov}[\mathbf{m}] = \left[[\mathbf{G}^T\mathbf{G}]^{-1}\mathbf{G}^T\right] \sigma_d^2 \left[[\mathbf{G}^T\mathbf{G}]^{-1}\mathbf{G}^T\right]^T = \sigma_d^2 (\mathbf{G}^T\mathbf{G})^{-1}. \quad (10)$$

where $\mathbf{G}^T\mathbf{G}$ is invertible in this overdetermined inverse problem. The data resolution matrix for the overdetermined inverse problem $\mathbf{N} = \mathbf{G}[\mathbf{G}^T\mathbf{G}]^{-1}\mathbf{G}^T = \mathbf{I}$ indicates that the prediction error can be ignored in the inversion (Menke, 2012, p. 70). The single coda waveform can be described by equation (5). Since we use the corrected coda waveforms in the inversion and do not know the measurement error, the variance estimated from the difference between the coda waveform and the best fitting curve by equation (5) is used as the data variance,

$$\sigma_d^2 = \sum_{k,i,j} (\hat{b}_{ij}(t_k) - C_{ij} - \frac{-2\pi f}{Q_{Cij}(f)} t_k)^2 / (N-1), \quad (11)$$

where N is the product of the number of points in each discrete time series and the number of coda waveforms. In each frequency range, the estimated source and station amplitude term errors are of order 10^{-2} and the sourceside and stationside attenuation terms are of order 10^{-4}. The formal relative errors are thus about 1% of the best fitting attenuation terms, although this should be considered a lower error bound because it does not take into account the possibility of systematic (correlated) errors in the data, such as might be generated by 3-D attenuation structure not fully modeled by source and station amplitude terms alone.

4. Results

In total we obtained 16,318 measurements from 642 events with catalog magnitudes between 1.8 and 5.4 at 105 stations. The numbers of seismograms are 14,781, 14,781, 14,909, and 8,244 for the frequency bands centered at 1.5, 3, 6, and 12 Hz, respectively.

4.1. Coda Magnitude and Coda Spectra

Coda waves are less affected by the source radiation pattern and directivity than direct waves, and thus coda-derived magnitudes are potentially more reliable and stable than those computed using other methods. At long lapse times, coda waves sample and average a large volume surrounding the source and receiver region. In equation (7), the source amplitude term is a measure of the source radiated energy at a particular frequency (Aki, 1969; Baltay et al., 2010; Mayeda & Walter, 1996, 2003, Sens-Schönfelder & Wegler, 2006), which can be used to compute the source magnitude or source spectra.

In the inversion, there is a trade-off between the source and station amplitude terms and the sourceside attenuation and the stationside attenuation terms (i.e., if we remove a constant from the source amplitude terms and add it to the station amplitude terms, the misfit shown in equation (8) for the inverse problem remains the same). However, the relative differences in the terms among each set are resolved, even if their mean values are uncertain because of the source versus station trade-off. We can resolve the trade-off by setting the

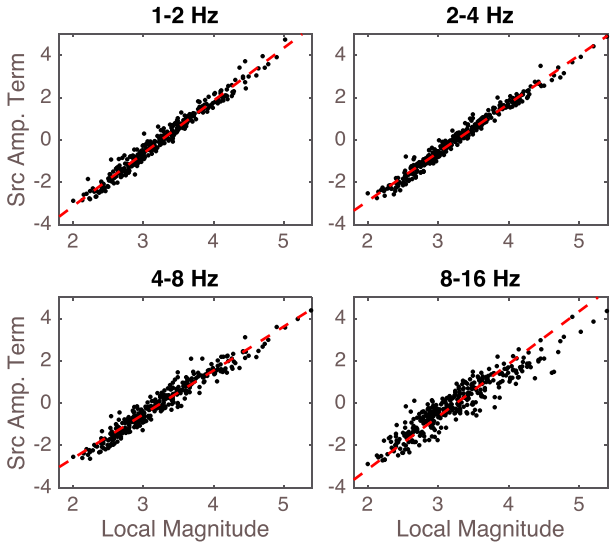

Figure 3. Uncorrected demeaned source amplitude terms versus catalog magnitudes at 1–2, 2–4, 4–8, and 8–16 Hz frequency bands. The red dashed lines show the best fitting linear regression between source amplitude terms and local magnitudes.

mean of one set of terms to zero, which will maximize the signal in the other set of terms. For example, we can remove the mean of the source-side attenuation terms and add it to the stationside attenuation terms and then compute station-specific coda-Q, which can be compared with the conventional SSMEM method. Sens-Schönfelder and Wegler (2006) use a similar method to solve for coda magnitude assuming the logarithmic average of the station terms is zero at all frequency ranges and then fit the source spectra by applying the omega-square model. Here we also remove the absolute amplitudes from the source terms and Figure 3 shows the source amplitude terms at different frequency bands. At the low-frequency band passes (1–2 and 2–4 Hz), the source amplitude terms scale linearly with catalog magnitude (i.e., larger source amplitude terms for larger earthquakes), as expected given that these two frequency ranges are well below the corner frequencies of most earthquakes in our data set. At frequencies above 4 Hz, the source amplitude terms no longer scale linearly, because the effect of earthquake corner frequency can no longer be ignored.

For small earthquakes ($M_L \leq 3.5$), the magnitudes listed in the catalog are the local magnitudes (M_L) rather than the moment magnitudes (M_W). Previous studies have indicated that $M_W \neq M_L$ (e.g., Hutton et al., 2010; Ross et al., 2016; Shearer et al., 2006; Trugman & Shearer, 2017). Before calibrating the source amplitude term to coda spectra, we need to compute the moment (M_0) for each event as our first step. Here we follow the method in Shearer et al. (2006). At low frequency (1–2 Hz), we first perform a linear regression between catalog magnitude M_L and source amplitude terms s: $M_L = as + b$. Since we use the energy densities of the seismograms and the moment is proportional to the low-frequency amplitude, the source amplitude terms scale linearly with log moment as $\log_{10}(M_0) = s/2 + C$ with scaling factor 0.5. The moment magnitude M_W (Kanamori, 1977) may be expressed as

$$M_W = \frac{2}{3}\log_{10} M_0 - 10.7 \tag{12}$$

where the moment M_0 is in N m. Finally, the source amplitude term of each event is converted to moment by assuming that $M_L = M_W$ at $M_W = 3.5$, consistent with recent results of Ross et al. (2016). We estimate the

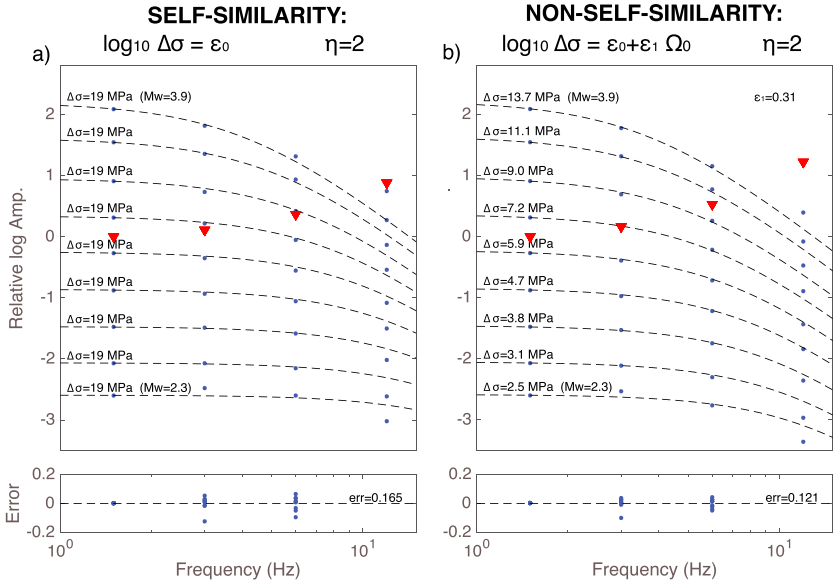

Figure 4. Empirical Green's function (EGF)-corrected, stacked source spectra from the source amplitude terms at 1–2, 2–4, and 4–8 Hz for (a) self-similar and (b) non-self-similar source models and their misfit with respect to a Brune-type source spectrum. The blue dots indicate the EGF-corrected source amplitude terms. Red triangles show the EGF. The black dashed lines indicate the theoretical source models.

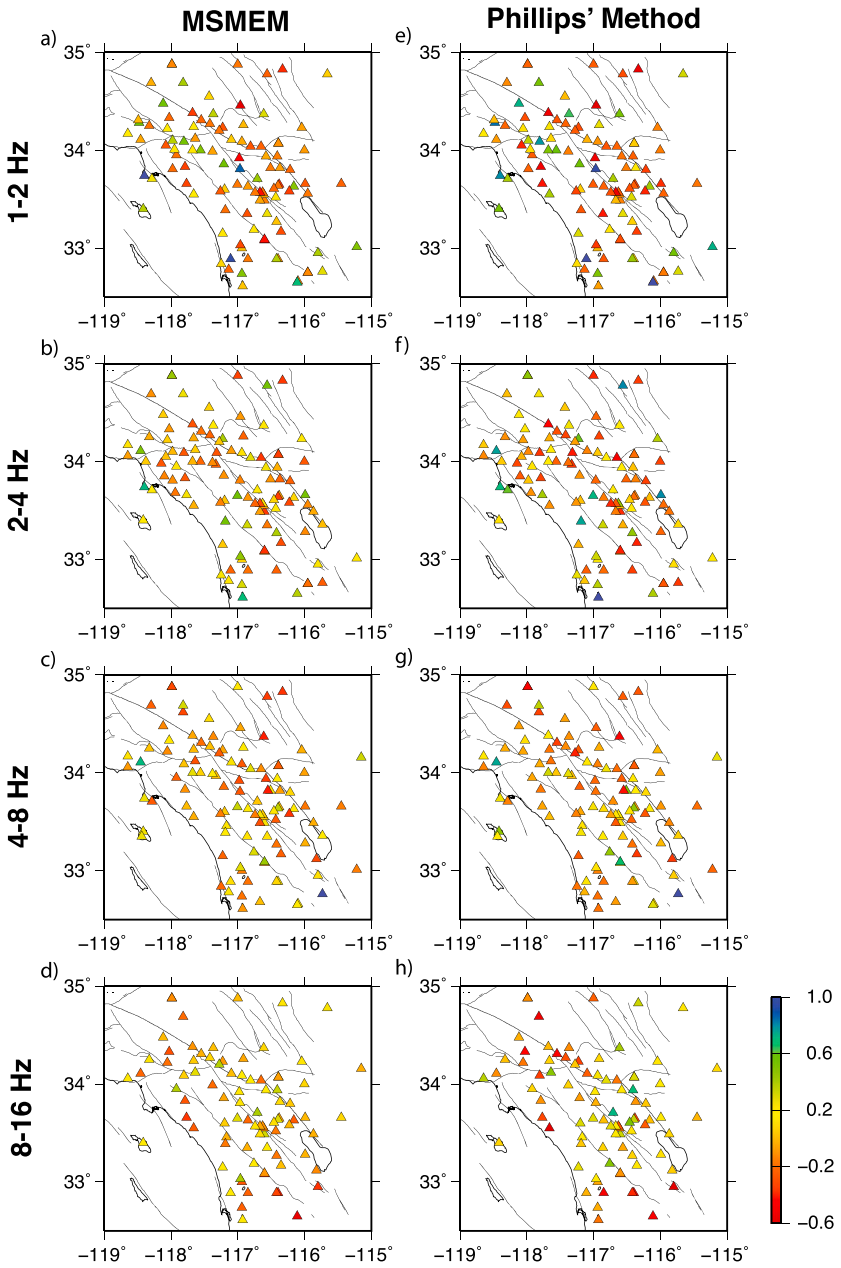

Figure 5. Comparisons of site amplification terms between our MSMEM and the method of Phillips and Aki (1986). The colors show the site amplification (log 10) relative to the 'average station,' with amplification factors ranging from 0.25 (dark red) to 10 (dark blue). Panels (a)–(d) show the site amplification effect from MSMEM at 1–2, 2–4, 4–8 and 8–16 Hz; (e)–(h) show results from the method of Phillips and Aki (1986). MSMEM = Multiple Station and Multiple Event Method.

moment M_0 as a function of catalog moment M_L expressed as,

$$M_0 = 10^{1.26(M_L-3.5)}1.43 \times 10^{14}\ \text{Nm} \tag{13}$$

Our observed scaling between M_L and $\log_{10}(M_0)$ is 1.26, which is within the range of 1.0 to 1.5 found in previous studies. Ben-Zion and Zhu (2002) obtained 1.0 for $M_L < 3$ events and 1.34 for $3.5 < M_L < 6.0$in southern California, and Bakun (1984) estimated 1.2 for $1.5 \leq M_L < 3.5$ events and 1.5 for $3.0 < M_L < 6.0$events in central California. Scaling factors in other studies include 1.0 for $M_L < 3.7$ by Abercrombie (1996), 1.04 for $1.5 \leq M_L \leq 3.1$ by Shearer et al. (2006), 1.1 for $1.5 \leq M_L \leq 4$ by Hawthorne et al. (2017), 1.22 for $0 \leq M_L \leq 4$ by Ross et al. (2016), and 1.5 for $1.8 \leq M_L \leq 3.4$ by Prieto et al. (2004). In general, larger scaling factors are expected for larger earthquakes where M_L and M_W are in better agreement (see Figure 9.25 from ; Shearer,

Table 1
Misfit Error Table of the Inversion Problem for All the Q_C Models

	1–2 Hz	2–4 Hz	4–8 Hz	8–16 Hz
No Q_C	0.0367	0.0391	0.0415	0.0639
Uniform Q_C	0.0248	0.0206	0.0191	0.0241
Sourceside Q_C	0.0245	0.0203	0.0187	0.0229
Stationside Q_C	0.0244	0.0202	0.0186	0.0231
Bothside Q_C	0.0241	0.0199	0.0180	0.0214

2009), and this is seen in the observed factors of 1.39 for $3 \leq M_L \leq 7$ events by Archuleta et al. (1982) and 1.5 for $3 \leq M_L \leq 7$ by Thatcher and Hanks (1973). Note that our coda study includes larger earthquakes (112 $M_L \geq 3.5$ events and 69 $M_L \geq 4.0$ events than the $1.5 \leq M_L \leq 3.1$ range in the *P* wave spectral study of Shearer et al. (2006)).

Differences in the source amplitude terms as a function of frequency contain information about the source spectra. However, because of the trade-off between the average source and station amplitude terms, the source amplitude terms at a given frequency only resolve the relative differences among the events and cannot be used directly to estimate the source spectrum of individual events by comparing the terms at different frequencies. To resolve this ambiguity, we apply the multiple-event empirical Green's function (EGF) approach used in spectral analysis of direct phases (e.g., Oth et al., 2011; Shearer et al., 2006). We stack the source amplitude terms at 0.2 increments in calibrated moment magnitude bins from $M_W = 2.3$ to 3.9 for the frequency bands centered at 1.5, 3, 6, and 12 Hz, respectively. Following Shearer et al. (2006), we estimate an EGF spectrum that will bring the stacked source amplitude terms into agreement with a theoretical model of the source spectra. Specifically, we minimize the L2-norm residual between the EGF-corrected stacked spectra and a self-similar Brune-type circular crack model (Brune, 1970; Madariaga, 2007). The amplitude of source spectra model is expressed as

$$S(f) = \frac{2\Omega_0}{1 + (f/f_c)^{\eta}}, \tag{14}$$

where Ω_0 is the long-period displacement amplitude, f is the frequency, f_c is the corner frequency, and 2 is the scaling factor from displacement to the energy densities. The corner frequency in the source model related to the moment and the stress drop is expressed as (Abercrombie, 1995; Madariaga, 1976; Shearer et al., 2006),

$$f_c = \frac{0.42\beta}{(M_0/\Delta\sigma)^{1/3}} \tag{15}$$

where β is the *S* wave velocity, M_0 is the moment, $\Delta\sigma$ is the stress drop, and β is shear-wave velocity, assumed here a constant 3.5 km/s.

Assuming a self-similar constant stress drop model, we perform a grid search over stress drop to determine the EGF that minimizes the difference between the EGF-corrected stacked spectra and the synthetic spectra of the Brune-type source model. Following Trugman and Shearer (2017), we also experiment with models in which stress drop varies as a function of moment, specifically as

$$\log_{10} \Delta\sigma = \epsilon_0 + \epsilon_1 S(0) \tag{16}$$

where $S(0)$ is the long-period displacement amplitude (proportional to moment), ϵ_0 and ϵ_1 are two model parameters to describe the scaling between moment and stress drop.

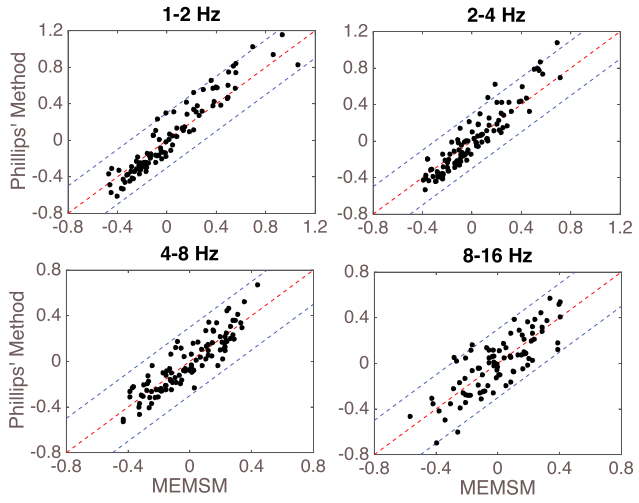

Figure 6. Comparisons of site amplification between our MSMEM and the method of Phillips and Aki (1986) at 1–2, 2–4, 4–8, and 8–16 Hz. The reference red and blue dashed lines show identical values and differences of ±0.3, respectively. MSMEM = Multiple Station and Multiple Event Method.

Figure 4 shows results for both the self-similar and non-self-similar scaling models. Results for the 8–16 Hz frequency range are problematic (i.e., yield poor fits), most likely a result of the poorer signal-to-noise in this band and the fact that it is difficult to use a single center frequency for plotting purposes when many of the earthquake corner frequencies are in this range. Consequently, we only use the 1–2, 2–4, and 4–8 Hz bands to fit the source spectra. The best fitting ω^{-2} Brune-type stress drop for the self-similar model is 19 MPa, which is higher than the average stress drop seen in previous studies. However, the best fitting ω^{-2} Brune-type stress drop for the non-self-similar model ranges from 2.5 to 13.7 MPa with scaling parameter $\epsilon_1 = 0.31$, which roughly agrees with results for the San Jacinto region of southern California in Trugman and Shearer (2017). Compared to the self-similar source model ($err = 0.165$), the non-self-similar source model yields a better fit ($err = 0.121$; see Figures 4a and 4b). However, the model fits are far from exact, and there is a fundamental trade-off between the non-self-similar scaling parameter (ϵ_1) and the assumed high-frequency fall-off rate (η) (Trugman & Shearer, 2017). Thus,

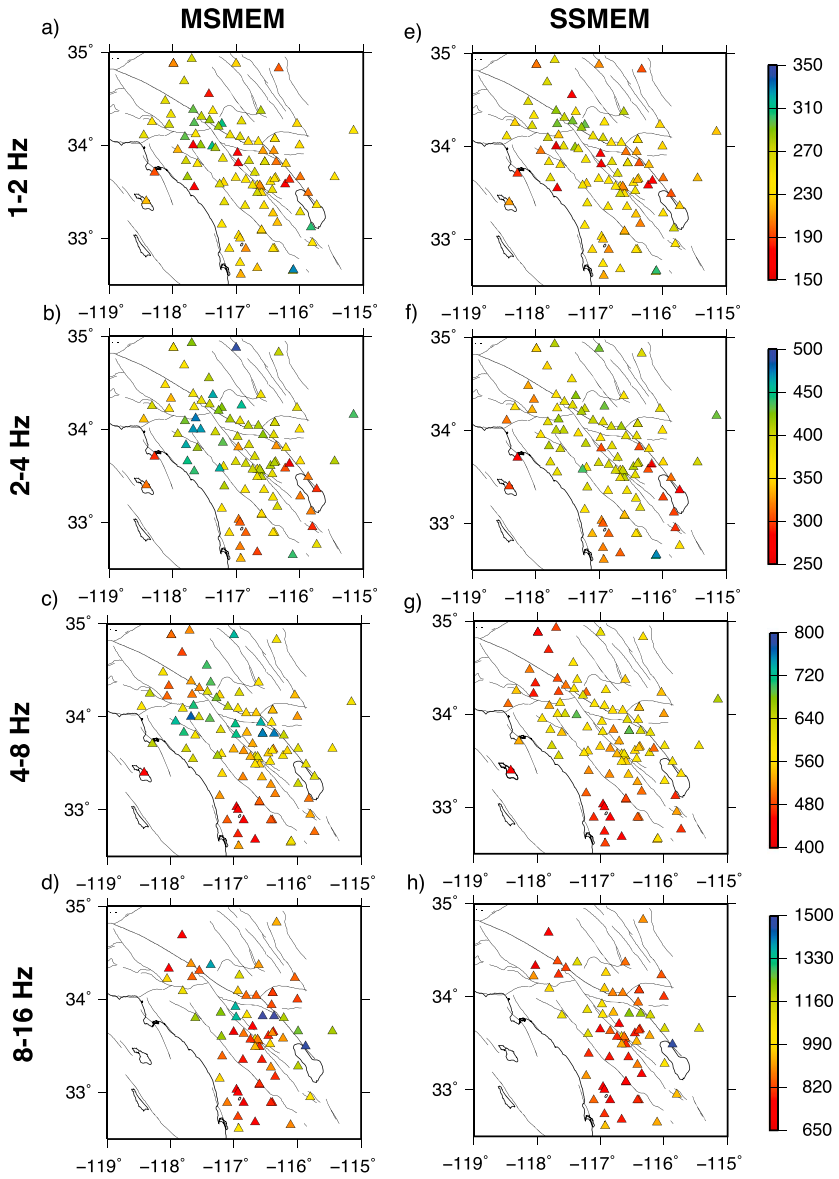

Figure 7. Spatial distribution of the stationside coda attenuation Q_C at 1–2, 2–4, 4–8, and 8–16 Hz. The scale of Q value is shown at the right-hand side of each row.

the source spectral results shown here should be considered tentative until a more complete analysis can be performed that considers all of the model uncertainties and parameter trade-offs. However, uncertainties in the source spectral calibration do not affect the accuracy of the amplitude and coda decay terms that are the main focus of this paper. We plan further study of coda-based source spectral estimates and comparisons to direct phase spectral analyses in future work.

4.2. Site Amplification

As mentioned in the Coda Magnitude section, the mean value of the station amplitude terms is removed, which means that the station amplitude terms are relative to the "average station" (Phillips & Aki, 1986,Su & Aki, 1995; Su et al., 1991, 1992). Since the smoothed energy densities are used in this study, we apply a scaling factor of 0.5 to correct them to amplitude site amplification factors. Figures 5a–5d show the site amplification factors at different frequency bands. To validate the accuracy of our approach, we compare our results with another coda-based method to determine site amplification developed by Phillips and Aki (1986), which was used by later studies in southern California (i.e., Su et al., 1991, 1992; Su & Aki, 1995). Their method is also

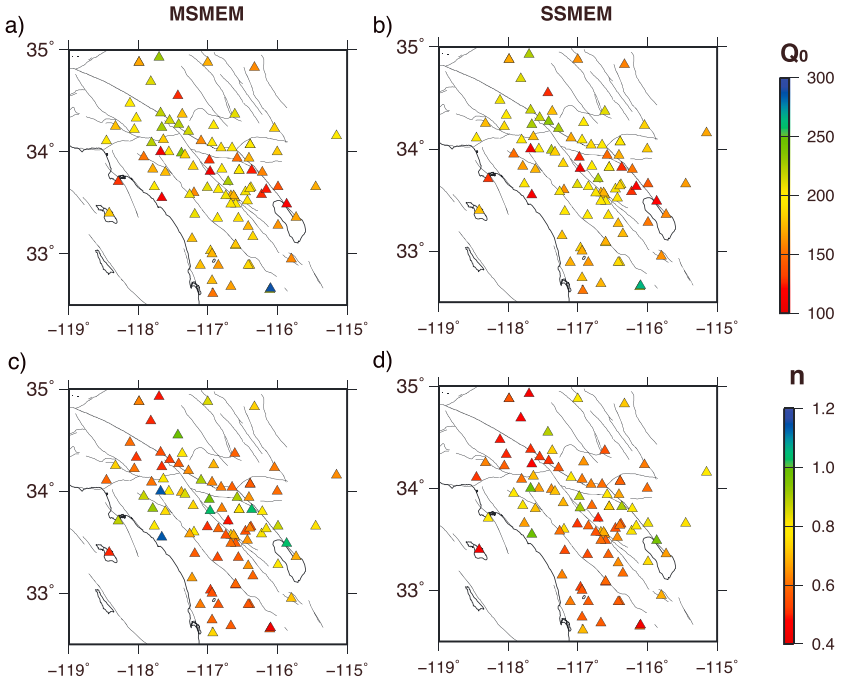

Figure 8. Spatial distribution of the stationside coda attenuation Q_C at 1 Hz and power n. The scale of Q_C and n values are shown at the right-hand side of each panel. (a) and (b) illustrate the Q_C distributions for MSMEM and SSMEM, respectively. (c) and (d) show the n distributions for MSMEM and SSMEM, respectively. MSMEM = Multiple Station and Multiple Event method; SSMEM = Single Station and Multiple Event Method.

based on equation (3); given the frequency and lapse time, the logarithmic root-mean-square coda energy can be written as

$$e_{ij}(t_k) = s_i + r_j + c_{ij}(t_k), \tag{17}$$

where $c_{ij}(t_k)$ is a constant among all the records given the lapse time t_k, which assumes a uniform spacial distribution of the coda attenuation Q_C. The uniform coda attenuation Q_C can explain most of the observations compared to the stationside and sourceside variant Q_C (see Table 1). This assumption differs from our MSMEM

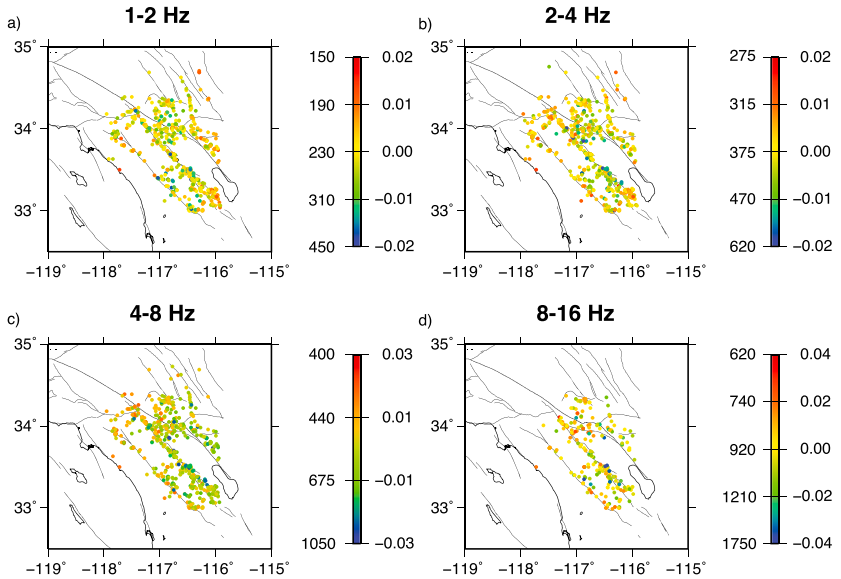

Figure 9. Spatial distribution of the sourceside coda attenuation terms $-2\pi f/Q_C^S$ or Q_C^S at (a) 1–2, (b) 2–4, (c) 4–8, and (d) 8–16 Hz. The scale of the attenuation terms is shown at the right-hand side of each subplot. The color bar is linearized in $-2\pi f/Q_C^S$ and corresponding Q_C^S.

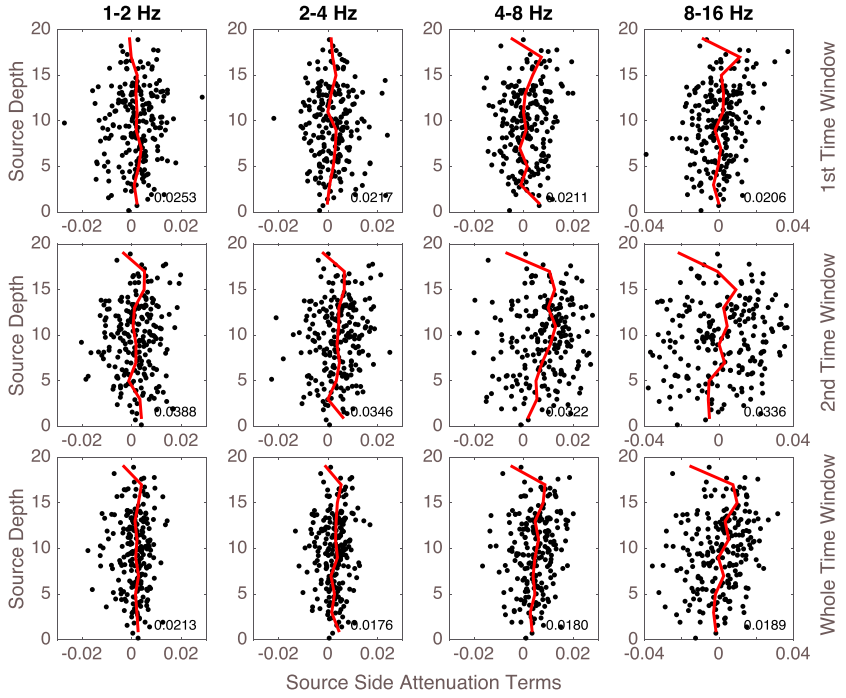

Figure 10. Relation between the sourceside coda attenuation terms $-2\pi f/Q_C^S$ with the source depths at 1–2, 2–4, 4–8, and 8–16 Hz. The first row shows sourceside coda attenuation terms for the time window 50–70 s, the second row shows the results for the time window 70–90 s, and the third row shows the results for the time window 50-90 s. Each black dot represents an event and red lines indicate the median values of the sourceside coda attenuation terms binned at 0.2 intervals in coda magnitude.

approach and may cause some differences in the results. We compute an average of e_{ij} over all the available stations for the ith source and this average ($\bar{e}_{ij}^{ik}(t_k)$) is removed from the root-mean-square energy e_{ij} with the fixed ith source, that is,

$$\frac{1}{2}\left[e_{ij}(t_k) - \bar{e}_{ij}^{ik}(t_k)\right] = r_j - \bar{r}, \tag{18}$$

where $\bar{r}$ is the average site amplification and the scaling factor 1/2 is used to correct the results to amplitude site amplification. Equation (18) can be written in the form $\mathbf{d} = \mathbf{Gm}$. The $\mathbf{G}$ is a large, sparse matrix, so we apply the same least squares method. The results at different frequency bands are shown in Figures 5e–5h. In general, the results from the two methods are quite similar, as shown in Figure 6. The ratio of differences between the methods are less than 0.3 in log 10 scale, scaling factor 2, 100%, 99%, 95%, and 85% at 1–2, 2–4, 4–8, and 8–16 Hz, respectively. These comparisons indicate that our site amplification results are generally consistent with the method of Phillips and Aki (1986).

In Su et al. (1991, 1992), they pointed out the site amplification is related to the geology underlying the station. Our results are spatially consistent with their results. For instances, the stations on the Mesozoic granitic rocks or Pre-Cretaceous metamorphic rocks have low site amplification but gradually increase with frequency, which appears on the stations around the San Jacinto Fault Zone (−116.6°W, 33.5°N). At the centered frequency 1.5 Hz, the region around the northern end of the Chino Fault (−117.6°W, 34°N) and the southeastern region of the Salton Trough (−115.8 to −115.2°W, 33°N), which consist mainly of Cenozoic sediments, show the highest amplification and gradually decrease with frequency. Also, along the San Andreas fault, the site amplifications do not show systematic changes, which was also pointed out by Su et al. (1992).

4.3. Coda Attenuation

Coda attenuation Q_C is another important parameter in our method. We separate coda attenuation into two parts, sourceside attenuation (Q_C^S) and stationside attenuation (Q_C^R) (see equation (6)). Considering

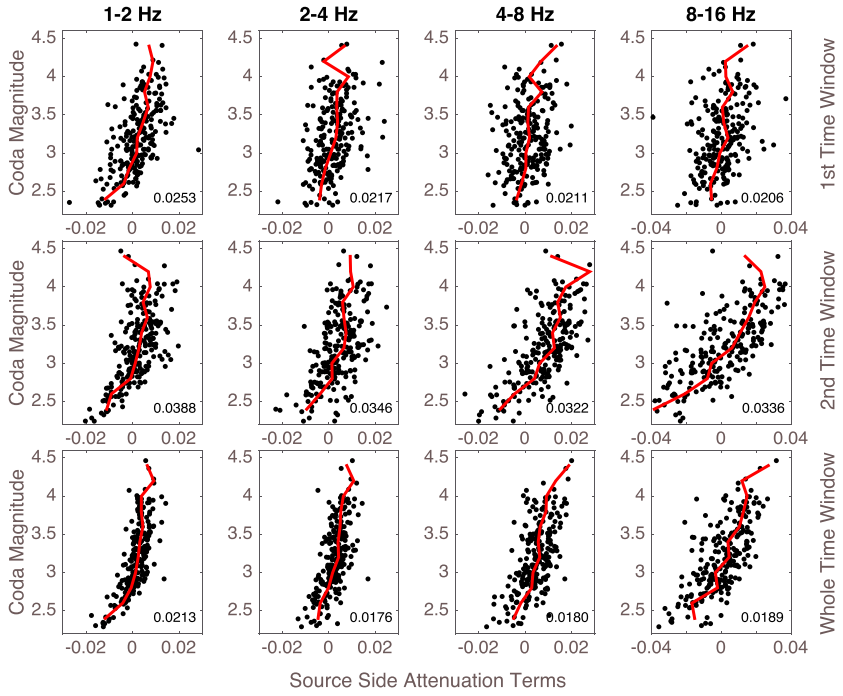

Figure 11. Relation between the sourceside coda attenuation terms $-2\pi f/Q_C^S$ with the coda magnitudes at 1–2, 2–4, 4–8, and 8–16 Hz. The first row shows the results of sourceside coda attenuation terms for the time window 50–70 s, the second row shows the results for the time window 70–90 s, and the third row shows the results for the time window 50–90 s. Each black dot shows the result for each event, and red lines indicate the median values of the sourceside coda attenuation terms binned at 0.2 interval in coda magnitude.

the trade-off between these two terms, to view the variation in sourceside attenuation and stationside attenuation, we rewrite the attenuation terms in the new form,

$$Q_{Ci}^{S\,-1} + Q_{Cj}^{R\,-1} = \delta Q_{Ci}^{S\,-1} + \delta Q_{Cj}^{R\,-1} + \overline{Q_C^{-1}} \tag{19}$$

where $\bar{q}$ is the mean value of the total attenuation terms and δQ_{Ci}^{S-1} and δQ_{Cj}^{R-1} are perturbations to mean coda Q_C^{-1} on the sourceside and stationside, respectively. The reciprocal of the summation of the stationside variation (δQ_C^{R-1}) and the mean value ($\overline{Q_C^{-1}}$), which is the stationside coda attenuation (Q_C^R) has the same physical and mathematical meaning as in the conventional method (SSMEM). Similarly, we can define a sourceside attenuation term, Q_C^S, which is the reciprocal of the summation of the sourceside variation (δQ_C^{S-1}) and the mean value ($\overline{Q_C^{-1}}$), likely describes differences in scattering from heterogeneity close to the source regions.

To validate our approach, we compare our results with those from SSMEM, which measures the attenuation at each station recording multiple events. The measured coda attenuations are averaged and plotted at each station. As shown in Figure 7, the spatial variations in Q_C are similar for the different methods. Previous studies (e.g., Aki, 1980; Carcolé & Sato, 2010; Jin & Aki, 2005) have indicated the coda attenuation follows a frequency-dependent power law, $Q(f) = Q_0 f^n$. The results from MSMEM indicate that Q_0 and n are within the ranges 107–288 and 0.42–1.14, respectively. The results from SSMEM are in reasonable agreement, with Q_0 and η within the ranges 111–264 and 0.45–0.99, respectively. The spatial variations of Q_0 and n are also correlated between the methods, as shown in Figure 8. Although there are some differences, overall the results from MSMEM are consistent with SSMEM. In general our values of Q_0 and n agree with previous studies, which indicate Q_0 is within 100–500 and n within 0.4–1.3 (e.g., Carcolé & Sato, 2010; Jin & Aki, 1988, 2005; Mayeda, Koyanagi, & Aki, 1991; Singh & Herrmann, 1983; Yun et al., 2007).

In Figure 9, we show the spatial distribution of the removed mean sourceside attenuation terms $-2\pi f/Q_C^S$ at 1–2, 2–4, 4–8, and 8–16 Hz, respectively. The spatial patterns between sourceside attenuation and stationside attenuation at different frequency bands are similar but have some variation. As in the case of the site amplification results, the largest discrepancy appears for the frequency band 8–16 Hz, probably because of a low signal-to-noise ratio. On the other hand, the spatial variations of sourceside attenuation are not exactly

the same as the stationside variations, because the sources are located at different depths from 0 to 20 km. Figure 10 and Figures S1–S4 in the supporting information indicate that the sourceside attenuation is not related to the source depth. However, the sourceside attenuation shows positive correlation with the coda magnitudes (see Figure 11c). To examine this relationship, we compute the sourceside attenuation using the coda wave in the first-half time window (i.e., 50–70 s) and the second-half time window (i.e., 70–90 s), compared to the results within the whole-time window 50–90 s. The comparison of the two half-time windows indicates that the positive correlation is an artifact from the low signal-to-noise ratio at longer times. This positive correlation is stronger in the second time window than in the first time window and this effect is stronger for small events than larger events. The strongest positive correlation appears in the second time window at the frequency range 8–16 Hz, together with the most scattered results. The misfit errors for the second half-time window are systematically larger than the misfit errors for the first half-time windows. Because of this time dependence, it is likely that signal-to-noise issues are causing the apparent positive relation between coda-Q and coda magnitude.

5. Discussion

Geometrical spreading of coda waves is accounted for by the α term. Here we use $\alpha = 1.5$ for epicentral distances smaller than 100 km, assuming the 3-D diffusion case in a whole space, as in previous studies (Calvet & Margerin, 2013; Margerin et al., 1998). If instead we use $\alpha = 2.0$, assuming the single-scattering model, which is another widely applied value in coda attenuation studies (see ; Carcolé & Sato, 2010; Hiramatsu et al., 2000), there is little change in the relative values among the station, source, and attenuation terms, but there is a systematic shift in their absolute values. In this study, since we remove the mean value from the station amplitude terms and the sourceside attenuation terms, the shift occurs in the other terms and is -0.699 for the source amplitude terms (s_i) and 7.27×10^{-3} for the stationside attenuation terms ($-2\pi f / Q_C^R$). It should be noted that we use a fixed time window to measure the coda waves. Calvet and Margerin (2013) found that Q_C estimated by using SSMEM and $\alpha = 2$ is typically about 10% higher than when using $\alpha = 1.5$. Considering that they used a time window starting at twice the S travel time and a fixed lapse time, their results are consistent with ours. Overall, larger α values slightly increase the Q_C values, but since physically realistic α values are from 1 to 2, the variation of α does not affect the final results very much.

Previous studies (Calvet & Margerin, 2013) indicate that the choice of the time windows can affect the measurement of coda attenuation. To consider this issue, we test time windows of 30, 40, and 50 s. We find that compared to the 40-s case, the relative differences are small, that is, over 90% of the station and source amplitude terms have a difference smaller than 0.5 and sourceside and stationside Q_C^{-1} smaller than 0.001.This indicates that within the window length range of 30–50 s, the solutions are robust. Second, increasing the window length increases the measured Q_C, which was also reported by Calvet and Margerin (2013). To examine this effect, we keep the window length fixed at 40 s and change the starting lapse time to 60 and 70 s. We find that the measured Q_C systematically increases with the starting lapse time, which was also reported by some other studies, (Carcolé & Sato, 2010; Hiramatsu et al., 2000; Phillips & Aki, 1986; Rautian & Khalturin, 1978; Yoshimoto & Jin, 2008).

The physical meaning of coda attenuation Q_C, including the relative importance of scattering versus intrinsic attenuation, has been debated for some time. In principle, contributions to the coda come from within an ellipsoidal-shaped volume defined by the source-to-scatterer-to-station travel time. Relating differences in observed coda Q_C to variations in properties within this volume is not straightforward, but some clues about the source of coda Q_C variations are provided by mapping them to the stations or the source-receiver midpoint (Aki, 1996; Pulli, 1984; Roecker et al., 1982; Steck et al., 1989). Here we examine coda Q_C variations across southern California, as assigned both to the stations (Figure 7) and to the sources (Figure 9). These maps exhibit spatial coherence, which provides some reassurance that the observed variations are not caused by purely random coda fluctuations, but they often exhibit changes over shorter length scales than the size of the scattering ellipsoid. This indicates that the entire scattering volume does not contribute equally to coda Q_C variations, that changes in properties in the shallow crust beneath the stations and within seismically active regions are particularly important. In general, both the sourceside and stationside coda-Q results show common lower values around the Salton Sea, a geothermal region, consistent with previous coda at lower frequency (< 4 Hz) and direct-wave attenuation studies (Aki, 1996; Hauksson & Shearer, 2006). A difference between direct and coda wave studies is seen in the region of the Chino Basin and San Gabriel Valley, where

Table 2
Misfit Error Table From Removing Each Term on the Right Side of Equation (20)

	1–2 Hz	2–4 Hz	4–8 Hz	8–16 Hz
All terms included	0.0241	0.0199	0.0204	0.0214
No geometric spreading	0.4000	0.4006	0.4050	0.4046
No $\bar{q}$, δq^S, and δq^R	0.1696	0.2503	0.2869	0.3671
No $\bar{q}$	0.1625	0.2002	0.2667	0.3303
No δq^S and δq^R	0.0419	0.0376	0.0511	0.0772
No δq^S	0.0349	0.0311	0.0430	0.0570
No δq^R	0.0332	0.0303	0.0400	0.0647
No δs and δr	0.2607	0.2455	0.2355	0.2095
No δs	0.2271	0.2243	0.2247	0.1961
No δr	0.1128	0.0855	0.0755	0.0922

S wave attenuation (Q_S) is low (Hauksson & Shearer, 2006), which is consistent with our sourceside attenuation (see Figure 9); however, station coda-*Q* is high (Aki, 1996), also consistent with our results (see Figure 7).

In contrast to most previous studies, which focus on receiverside Q_C variations, here we consider two attenuation terms, sourceside attenuation (Q_C^S) and stationside attenuation (Q_C^R). Because any increase in the number of model parameters in an inversion should lead to a better fit, it is important to examine how misfit varies for different model parameter choices. Table 1 lists misfit errors for different coda-*Q* models, including purely sourceside and receiverside Q_C models. At lower frequencies (1–2 and 2–4 Hz), the stationside Q_C model fits better than the sourceside Q_C model, even though it has fewer parameters (i.e., the number of stations is smaller than the number of events). In contrast, at high frequency (8–16 Hz), the sourceside Q_C model fits better. However, even for the better fitting models, the differences in the misfit errors are very small, and using sourceside or stationside Q_C terms yields only slightly better fits than those achieved with a uniform Q_C model. Despite these small changes in fit, it is clear that the Q_C terms are measuring a real property of the crust, given the spatial coherence seen in the maps of Figures 7 and 9. The small changes in misfit occur because of the large scatter in coda decay for individual records and the fact that the average coda decay is mostly accounted for with the geometrical spreading term, such that Q_C is relatively large (i.e., $2\pi f/Q_C$ is consistently small).

To illustrate the importance of each part of equation (6), we rewrite the misfit function as,

$$err = \frac{\sqrt{\sum_{i,j,k}(\hat{e}_{ij}(t_k) + \alpha \log t_k - \bar{c} - \delta s_i - \delta r_j + \bar{q} + \delta q_i^S + \delta q_j^R)^2}}{\sqrt{\sum_{i,j,k} \hat{b}_{ij}^2(t_k)}}. \quad (20)$$

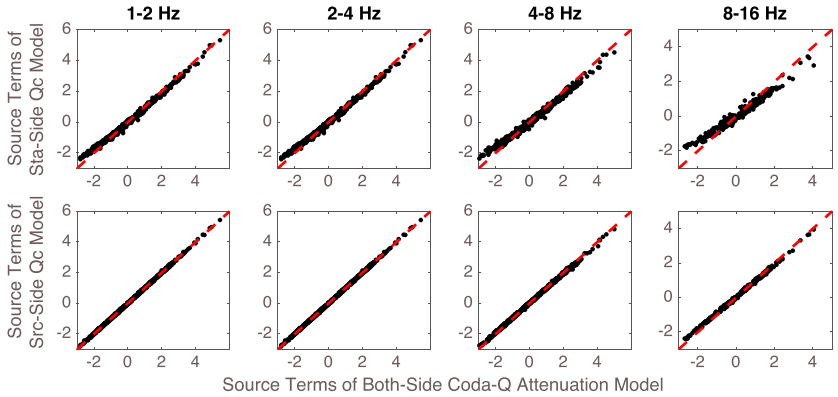

Figure 12. Comparisons of the source amplitude terms (top row) between bothside MSMEM and stationside MSMEM, and (bottom row) between bothside MSMEM and sourceside MSMEM at 1–2, 2–4, 4–8, and 8–16 Hz, respectively. The top four figures show comparisons of source amplitude terms between bothside MSMEM and stationside MSMEM; the bottom figures show comparisons of station amplitude terms between bothside MSMEM and sourceside MSMEM. Each black dot represents an event, and the red dashed lines indicate identical results.

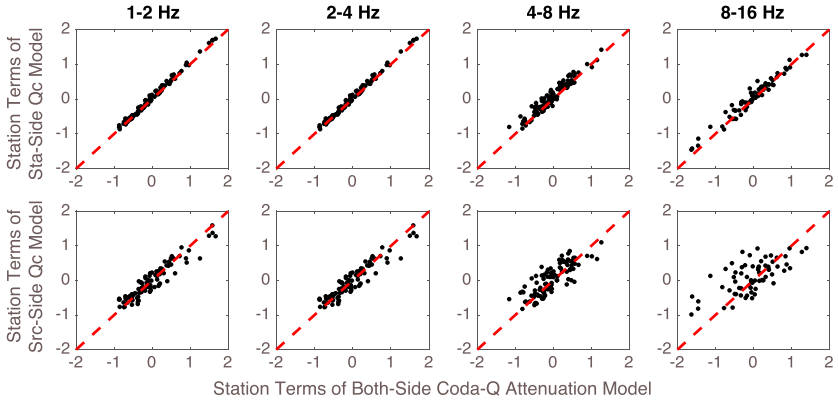

Figure 13. Comparisons of the station amplitude terms from (top row) bothside MSMEM and stationside MSMEM, and (bottom row) bothside MSMEM and sourceside MSMEM, the same as in Figure 12.

where the $\bar{c}$ is the mean value of the total source (s) and station (r) amplitude terms, δs and δr are the removed mean source and station amplitude terms, similarly, $\bar{q}$ is the mean value of the total Q_C terms, and δq^S and δq^R are the removed mean sourceside and stationside Q_C terms. We remove one term on the right-hand side from equation (20) each time and compute the misfit errors, which are listed in Table 2. The geometric spreading term is the most important part of the inverse problem, and the source amplitude term, station amplitude term, and the mean Q_C term are important in the inversion. Considering the number of events is much larger than than the number of stations, the residuals for the synthetics containing only the source amplitude terms are smaller than those containing only the station amplitude terms, as expected. For the Q_C terms, similar to Table 1, the uniform mean Q_C terms mostly explain the observations, and including the sourceside and/or stationside Q_C terms does not improve the fit very much. Also, comparing the misfit errors after removing different Q_C terms, it is difficult to tell whether the sourceside or stationside Q_C term dominates the inversion, so we prefer the bothside Q_C model in our MEMSM from both the physical and mathematical explanations.

When solving equation (6), we only keep the stationside attenuation terms. We find the attenuation Q_C is almost the same as the Q_C measured by SSMEM for each station with error less than 0.1%. However, our

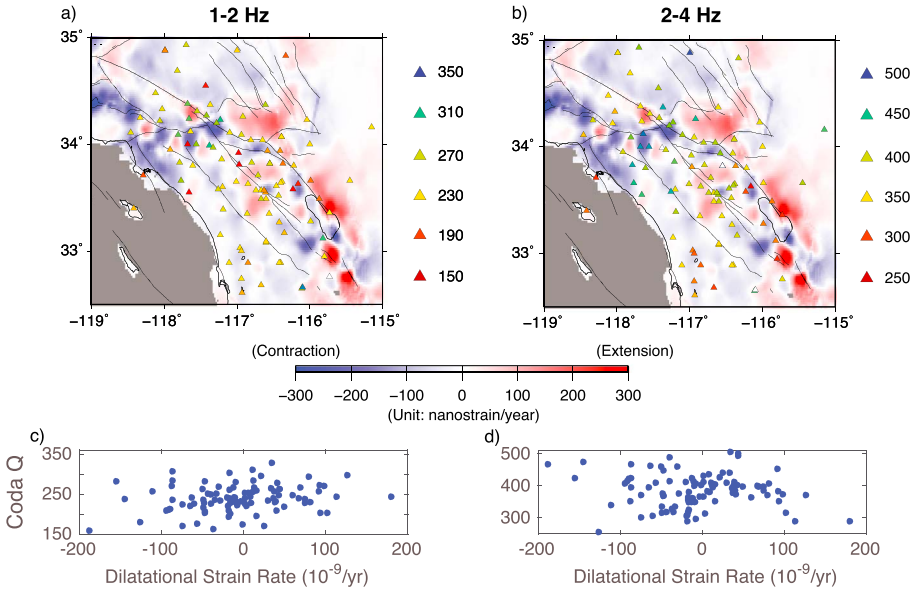

Figure 14. Comparisons of the coda attenuation Q_C with the dilatational strain rate in southern California at 1–2 and 2–4 Hz. Panels (a) and (b) show the spatial distribution of the dilatational strain rate together with the spatial distribution of the Q_C at 1–2 and 2–4 Hz. Panels (c) and (d) show the comparison of the Q_C and the interpolated dilatational strain rates at the same station locations.

MEMSM approach provides an additional three useful parameters, the source and station amplitude terms together with the sourceside Q_C. To validate that MEMSM is a consistent and robust method, we compare the source amplitude terms and station amplitude terms between the bothside Q_C attenuation model, the sourceside model, and the stationside model, as shown in Figures 12 and 13, respectively. Generally, the source and station amplitude terms are relatively consistent regardless of differing Q_C attenuation models, especially for the low-frequency bands (<8 Hz). For the high-frequency band (8–16 Hz), we find larger discrepancies between the bothside Q_C and stationside Q_C models for the source amplitude terms and between the bothside Q_C and sourceside Q_C models for the station amplitude terms. This is caused by the weaker signal-to-noise ratio in this frequency band, especially for small earthquakes. Also, analysis of the source amplitude terms indicates that the source spectra calibrated from the source amplitude terms are consistent for the low-frequency bands (<8 Hz) regardless of different Q_C attenuation models.

Jin and Aki (2005) point out the coincidence between low Q_C and high dilatational strain rate (<4 Hz) assuming the brittle-ductile interaction hypothesis of earthquake loading by plate-driving force in Japan. Here we examine this coincidence in southern California. The strain rate data are derived from the Community Geodetic Model (CGMl; Sandwell & Wessel, 2016). Similar to Jin and Aki (2005), we compute the dilatational strain rate ($e_{xx}+e_{yy}$) (see Figures 14a and 14b). To better illustrate the comparison between Q_C and dilatational strain rate, we interpolate the dilatational strain rate based on the station locations (see Figures 14c and 14d). From this comparison of Q_C and dilatational strain rate in southern California, we do not find a clear correlation between Q_C and dilatational strain rate. In Japan, the Niigata-Kobe Tectonic Zone (NKTZ) is a high strain rate zone where the dilatational strain rate is an order of magnitude larger than the surrounding region and NKTZ is also a volcanic and geothermal region. However, in southern California, the background tectonics is strike slip, compared to the convergence tectonics in Japan. The shear strain rate is much larger than dilatational strain rate, and the dilatational strain rate is spatially smoother in southern California. These factors may result in no coincidence between low Q_C and dilatation strain rate in southern California.

6. Conclusion

In summary, based on a standard model for coda energy decay, we invert for separate source, station, and coda attenuation terms in the logarithmic domain. We develop a method to use a representative expression of coda waves as the data vector to greatly reduce the size of the least squares inverse problem.Applying our method to data from southern California in four different frequency bands, we obtain source amplitude terms related to coda magnitude and source spectra, station amplitude terms related to site effects, and coda-*Q* terms related to lateral variations in scattering and attenuation. Our approach provides an efficient, robust, and self-consistent method to simultaneously determine coda-*Q*, earthquake magnitude, and site amplification.

Appendix A: Proof of Equal Solutions

The least squares solution for overdetermined inverse problem $\mathbf{b} = \mathbf{Gm}$ is,

$$\mathbf{m} = (\mathbf{G}^\mathbf{T}\mathbf{G})^{-1}(\mathbf{G}^\mathbf{T}\mathbf{b}). \tag{A1}$$

For an arbitrary coda waveform, equation (4) can be expressed as

$$\begin{bmatrix} b(t_1) \\ b(t_2) \\ \vdots \\ b(t_k) \end{bmatrix} = \begin{bmatrix} a(t_1) \\ a(t_2) \\ \vdots \\ a(t_k) \end{bmatrix} + \begin{bmatrix} \log(t_1) \\ \log(t_2) \\ \vdots \\ \log(t_k) \end{bmatrix} \alpha = \begin{bmatrix} 1 \\ 1 \\ \vdots \\ 1 \end{bmatrix} C + \begin{bmatrix} t_1 \\ t_2 \\ \vdots \\ t_k \end{bmatrix} q = \begin{bmatrix} 1 & t_1 \\ 1 & t_2 \\ \vdots & \\ 1 & t_k \end{bmatrix} \begin{bmatrix} C \\ q \end{bmatrix} \tag{A2}$$

$$\mathbf{b} = \mathbf{Gm}. \tag{A3}$$

And the corrected data vector is expressed as

$$\hat{\mathbf{b}} = \mathbf{G}(\mathbf{G}^\mathbf{T}\mathbf{G})^{-1}\mathbf{G}^\mathbf{T}\mathbf{b}. \tag{A4}$$

The difference vector n between the data vector $\mathbf{b}$ and corrected data vector $\hat{\mathbf{b}}$ is defined as

$$\mathbf{n} = \mathbf{b} - \hat{\mathbf{b}} = \mathbf{b} - \mathbf{G}(\mathbf{G}^\mathbf{T}\mathbf{G})^{-1}\mathbf{G}^\mathbf{T}\mathbf{b}. \tag{A5}$$

The difference vector $\mathbf{n}$ yields $\mathbf{G}^\mathbf{T}\mathbf{n} = \mathbf{0}$. Given that $(\mathbf{G}^\mathbf{T}\mathbf{G})$ is invertable, which is valid in this study, the proof is as below:

$$\mathbf{G}^\mathbf{T}\mathbf{n} = \mathbf{G}^\mathbf{T}\mathbf{b} - \mathbf{G}^\mathbf{T}\mathbf{G}(\mathbf{G}^\mathbf{T}\mathbf{G})^{-1}\mathbf{G}^\mathbf{T}\mathbf{b} = \mathbf{G}^\mathbf{T}\mathbf{b} - \mathbf{G}^\mathbf{T}\mathbf{b} = \mathbf{0} \tag{A6}$$

$$= [\mathbf{g}_1^\mathbf{T} \quad \mathbf{g}_2^\mathbf{T}]\mathbf{n} = \begin{bmatrix} 0 \\ 0 \end{bmatrix}, \tag{A7}$$

where, $\mathbf{g}_1^\mathbf{T} = [1 \quad 1 \quad \cdots \quad 1]^T$ and $\mathbf{g}_2^\mathbf{T} = [t_1 \quad t_2 \quad \cdots \quad t_k]^T$.

The solution for the inverse problem $\hat{\mathbf{b}} = \mathbf{G}\hat{\mathbf{m}}$ is,

$$\hat{\mathbf{m}} = (\mathbf{G}^\mathbf{T}\mathbf{G})^{-1}(\mathbf{G}^\mathbf{T}\hat{\mathbf{b}}) = (\mathbf{G}^\mathbf{T}\mathbf{G})^{-1}\mathbf{G}^\mathbf{T}(\mathbf{b} - \mathbf{n}) = (\mathbf{G}^\mathbf{T}\mathbf{G})^{-1}\mathbf{G}^\mathbf{T}\mathbf{b} - (\mathbf{G}^\mathbf{T}\mathbf{G})^{-1}\mathbf{G}^\mathbf{T}\mathbf{n} \tag{A8}$$

$$= (\mathbf{G}^\mathbf{T}\mathbf{G})^{-1}\mathbf{G}^\mathbf{T}\mathbf{b} = \mathbf{m}. \tag{A9}$$

This solution indicates that for any single coda wave, the solutions for both raw data vector and corrected data vector are the same. Furthermore, we prove that this conclusion is still valid for multiple traces as equation (6). The equation (6) can be rewritten as

$$\begin{bmatrix} \mathbf{b}_{11} \\ \mathbf{b}_{12} \\ \vdots \\ \mathbf{b}_{nm} \end{bmatrix} = \left[\begin{array}{cccc|cccc|cccc} \mathbf{g}_1 & 0 & \cdots & 0 & \mathbf{g}_1 & 0 & \cdots & 0 & \mathbf{g}_2 & 0 & \cdots & 0 \\ \mathbf{g}_1 & 0 & \cdots & 0 & 0 & \mathbf{g}_1 & \cdots & 0 & 0 & \mathbf{g}_2 & \cdots & 0 \\ \vdots & \vdots & \vdots & \vdots & \vdots & \vdots & \vdots & \vdots & \vdots & \vdots & \vdots & \vdots \\ 0 & 0 & \cdots & \mathbf{g}_1 & 0 & 0 & \cdots & \mathbf{g}_1 & 0 & 0 & \cdots & \mathbf{g}_2 \end{array}\right] \begin{bmatrix} \mathbf{s} \\ \mathbf{r} \\ \mathbf{q} \end{bmatrix} \tag{A10}$$

$$\mathbf{b} = \tilde{\mathbf{G}}\mathbf{m} \tag{A11}$$

where $\tilde{\mathbf{G}}$ is used to distinguish from $\mathbf{G}$ in equation (A3), the vector $\mathbf{g}_1$ and $\mathbf{g}_2$ are the same as those in equation (A7), $\mathbf{s}$, $\mathbf{r}$, and $\mathbf{q}$ are the source amplitude term, station amplitude term, and attenuation term vectors. It is noted here that we do not separate the attenuation terms into the sourceside and stationside attenuation terms, since the proof is quite similar and the results here are valid. For an arbitrary single coda waveform, we have proven the difference vector $\mathbf{n} = \mathbf{b} - \hat{\mathbf{b}}$ yields $\tilde{\mathbf{G}}^\mathbf{T}\mathbf{n} = \mathbf{0}$. Here we will expand this result to multiple traces based on equation (6):

$$\tilde{\mathbf{G}}^\mathbf{T}\mathbf{n} = \left[\begin{array}{cccc} \mathbf{g}_1 & \mathbf{g}_1 & \cdots & 0 \\ 0 & 0 & \cdots & 0 \\ \vdots & \vdots & \cdots & \vdots \\ 0 & 0 & \cdots & \mathbf{g}_1 \\ \hline \mathbf{g}_1 & 0 & \cdots & 0 \\ 0 & \mathbf{g}_1 & \cdots & 0 \\ \vdots & \vdots & \cdots & \vdots \\ 0 & 0 & \cdots & \mathbf{g}_1 \\ \hline \mathbf{g}_2 & 0 & \cdots & 0 \\ 0 & \mathbf{g}_2 & \cdots & 0 \\ \vdots & \vdots & \cdots & \vdots \\ 0 & 0 & \cdots & \mathbf{g}_2 \end{array}\right] \begin{bmatrix} \mathbf{b}_{11} - \hat{\mathbf{b}}_{11} \\ \mathbf{b}_{12} - \hat{\mathbf{b}}_{12} \\ \vdots \\ \mathbf{b}_{nm} - \hat{\mathbf{b}}_{nm} \end{bmatrix} \tag{A12}$$

$$= \begin{bmatrix} \mathbf{g_1} & \mathbf{g_1} & \cdots & 0 \\ 0 & 0 & \cdots & 0 \\ \vdots & \vdots & \cdots & \vdots \\ 0 & 0 & \cdots & \mathbf{g_1} \\ \hline \mathbf{g_1} & 0 & \cdots & 0 \\ 0 & \mathbf{g_1} & \cdots & 0 \\ \vdots & \vdots & \cdots & \vdots \\ 0 & 0 & \cdots & \mathbf{g_1} \\ \hline \mathbf{g_2} & 0 & \cdots & 0 \\ 0 & \mathbf{g_2} & \cdots & 0 \\ \vdots & \vdots & \cdots & \vdots \\ 0 & 0 & \cdots & \mathbf{g_2} \end{bmatrix} \begin{bmatrix} \mathbf{n_{11}} \\ \mathbf{n_{12}} \\ \vdots \\ \mathbf{n_{nm}} \end{bmatrix} = \begin{bmatrix} \sum_i \mathbf{g_1 n_{1i}} \\ \sum_i \mathbf{g_1 n_{2i}} \\ \vdots \\ \sum_i \mathbf{g_1 n_{ni}} \\ \hline \sum_i \mathbf{g_1 n_{i1}} \\ \sum_i \mathbf{g_1 n_{i2}} \\ \vdots \\ \sum_i \mathbf{g_1 n_{im}} \\ \hline \sum_i \mathbf{g_2 n_{i1}} \\ \sum_i \mathbf{g_2 n_{i2}} \\ \vdots \\ \sum_i \mathbf{g_2 n_{im}} \end{bmatrix} = 0 \tag{A13}$$

$$\hat{\mathbf{m}} - \mathbf{m} = (\tilde{\mathbf{G}}^{\mathbf{T}}\tilde{\mathbf{G}})^{-1}\tilde{\mathbf{G}}^{\mathbf{T}}\hat{\mathbf{b}} - (\tilde{\mathbf{G}}^{\mathbf{T}}\tilde{\mathbf{G}})^{-1}\tilde{\mathbf{G}}^{\mathbf{T}}b = (\tilde{\mathbf{G}}^{\mathbf{T}}\tilde{\mathbf{G}})^{-1}\tilde{\mathbf{G}}^{\mathbf{T}}(\hat{\mathbf{b}} - \mathbf{b}) \tag{A14}$$

$$= (\tilde{\mathbf{G}}^{\mathbf{T}}\tilde{\mathbf{G}})^{-1}\tilde{\mathbf{G}}^{\mathbf{T}}\mathbf{n}=\mathbf{0} \tag{A15}$$

Here we have proven that when we used the corrected data vector $\hat{\mathbf{b}}$, we can get the same solution.

Acknowledgments
We would like to thank Carlos Alberto Vargas, another anonymous reviewer, and the Associate Editor for their comments, which have led to significant improvements in the paper. We also thank the personnel of the USGS/Caltech Southern California Seismic Network who pick and archive the seismograms and the Southern California Earthquake Center (SCEC) for distributing the data. This research was funded by NEHRP/USGS grant G18AP00024 and by SCEC grants 17041 and 18086. SCEC is funded by NSF Cooperative Agreement EAR-1033462 and USGS Cooperative Agreement G12AC20038. The refined catalog is available at http://scedc.caltech.edu/research-tools/downloads.html. The picked arrival times and seismograms are downloaded by using the Seismogram Transfer Program (STP), which is available at http://scedc.caltech.edu/research-tools/stp-index.html. The geologic map of California is available at http://maps.conservation.ca.gov/cgs/gmc/App/. Our Matlab codes of this improved coda-Q method and the source terms, station terms, sourceside, and stationside attenuation results are available at https://github.com/wew053/Coda-Q-Inversion.

References

Abercrombie, R. E. (1995). Earthquake source scaling relationships from −1 to 5 ML using seismograms recorded at 2.5-km depth. *Journal of Geophysical Research*, *100*(B12), 24,015–24,036.

Abercrombie, R. E. (1996). The magnitude-frequency distribution of earthquakes recorded with deep seismometers at Cajon Pass, southern California. *Tectonophysics*, *261*(1-3), 1–7.

Aki, K. (1969). Analysis of the seismic coda of local earthquakes as scattered waves. *Journal of Geophysical Research*, *74*(2), 615–631.

Aki, K. (1980). Scattering and attenuation of shear waves in the lithosphere. *Journal of Geophysical Research*, *85*(B11), 6496–6504.

Aki, K. (1996). Scale dependence in earthquake phenomena and its relevance to earthquake prediction. *Proceedings of the National Academy of Sciences of the United States of America*, *93*(9), 3740–3747.

Aki, K., & Chouet, B. (1975). Origin of coda waves: Source, attenuation, and scattering effects. *Journal of Geophysical Research*, *80*(23), 3322–3342.

Archuleta, R. J., Cranswick, E., Mueller, C., & Spudich, P. (1982). Source parameters of the 1980 Mammoth Lakes, California, earthquake sequence. *Journal of Geophysical Research*, *87*(B6), 4595–4607.

Aster, R. C., Slad, G., Henton, J., & Antolik, M. (1996). Differential analysis of coda Q using similar microearthquakes in seismic gaps. Part 1: Techniques and application to seismograms recorded in the Anza Seismic gap. *Bulletin of the Seismological Society of America*, *86*(3), 868–889.

Bakun, W. H. (1984). Seismic moments, local magnitudes, and coda-duration magnitudes for earthquakes in central California. *Bulletin of the Seismological Society of America*, *74*(2), 439–458.

Baltay, A., Prieto, G., & Beroza, G. C. (2010). Radiated seismic energy from coda measurements and no scaling in apparent stress with seismic moment. *Journal of Geophysical Research*, *115*, B08314. https://doi.org/10.1029/2009JB006736

Ben-Zion, Y., & Zhu, L. (2002). Potency-magnitude scaling relations for southern California earthquakes with $1.0 < ML < 7.0$. *Geophysical Journal International*, *148*(3), F1–F5.

Beroza, G. C., Cole, A. T., & Ellsworth, W. L. (1995). Stability of coda wave attenuation during the Loma Prieta, California, earthquake sequence. *Journal of Geophysical Research*, *100*(B3), 3977–3987.

Boatwright, J., Fletcher, J. B., & Fumal, T. E. (1991). A general inversion scheme for source, site, and propagation characteristics using multiply recorded sets of moderate-sized earthquakes. *Bulletin of the Seismological Society of America*, *81*(5), 1754–1782.

Brune, J. N. (1970). Tectonic stress and the spectra of seismic shear waves from earthquakes. *Journal of Geophysical Research*, *75*(26), 4997–5009.

Calvet, M., & Margerin, L. (2013). Lapse-time dependence of coda Q: Anisotropic multiple-scattering models and application to the Pyrenees. *Bulletin of the Seismological Society of America*, *103*(3), 1993–2010.

Carcolé, E., & Sato, H. (2010). Spatial distribution of scattering loss and intrinsic absorption of short-period *S* waves in the lithosphere of Japan on the basis of the Multiple Lapse Time Window Analysis of Hi-net data. *Geophysical Journal International*, *180*(1), 268–290.

Denieul, M., Sèbe, O., Cara, M., & Cansi, Y. (2015). M_W estimation from crustal coda waves recorded on analog seismograms. *Bulletin of the Seismological Society of America*, *105*(2A), 831–849.

Dewberry, S. R., & Crosson, R. S. (1995). Source scaling and moment estimation for the Pacific Northwest seismograph network using S-coda amplitudes. *Bulletin of the Seismological Society of America*, *85*(5), 1309–1326.

Eaton, J. P. (1992). Determination of amplitude and duration magnitudes and site residuals from short-period seismographs in Northern California. *Bulletin of the Seismological Society of America*, *82*(2), 533–579.

Eulenfeld, T., & Wegler, U. (2016). Measurement of intrinsic and scattering attenuation of shear waves in two sedimentary basins and comparison to crystalline sites in Germany. *Geophysical Journal International*, *205*(2), 744–757.

Eulenfeld, T., & Wegler, U. (2017). Crustal intrinsic and scattering attenuation of high-frequency shear waves in the contiguous United States. *Journal of Geophysical Research: Solid Earth*, *122*, 4676–4690. https://doi.org/10.1002/2017JB014038

Frankel, A., McGarr, A., Bicknel, J. , Mori, J. , Seeber, L. , & Cranswick, E. (1990). Attenuation of high-frequency shear waves in the crust: measurements from New York, South Africa, and southern California. *Journal of Geophysical Research*, *95*, 17,441–17,457.

Hauksson, E., & Shearer, P. M. (2006). Attenuation models (QP and QS) in three dimensions of the southern California crust: Inferred fluid saturation at seismogenic depths. *Journal of Geophysical Research*, *111*, B05302. https://doi.org/10.1029/2005JB003947

Hawthorne, J. C., Ampuero, J.-P., & Simons, M. (2017). A method for calibration of the local magnitude scale based on relative spectral amplitudes, and application to the San Juan Bautista, California, area. *Bulletin of the Seismological Society of America*, *107*(1), 85–96.

Hellweg, M., Spudich, P., Fletcher, J., & Baker, L. (1995). Stability of coda Q in the region of Parkfield, California: View from the US Geological Survey Parkfield dense seismograph array. *Journal of Geophysical Research*, *100*(B2), 2089–2102.

Herrmann, R. B. (1975). The use of duration as a measure of seismic moment and magnitude. *Bulletin of the Seismological Society of America*, *65*(4), 899–913.

Hiramatsu, Y., Hayashi, N., & Furumoto, M. (2000). Temporal changes in coda Q-1 and b value due to the static stress change associated with the 1995 Hyogo-ken Nanbu earthquake. *Journal of Geophysical Research*, *105*(3), 6141–6151.

Hoshiba, M. (1993). Separation of scattering attenuation and intrinsic absorption in Japan using the multiple lapse time window analysis of full seismogram envelope. *Journal of Geophysical Research*, *98*(B9), 15,809–15,824.

Huang, Z.-X., & Kisslinger, C. (1992). Coda-Q before and after the 1986 Andreanof Islands earthquake. *Pure and Applied Geophysics*, *138*(1), 1–16.

Huang, Z.-X., & Wyss, M. (1988). Coda Q before the 1983 Hawaii ($M_S = 6.6$) earthquake. *Bulletin of the Seismological Society of America*, *78*(3), 1279–1296.

Hutton, K., Woessner, J., & Hauksson, E. (2010). Earthquake monitoring in southern California for seventy-seven years (1932–2008). *Bulletin of the Seismological Society of America*, *100*, 423–446. https://doi.org/10.1785/0120090130

Ibanez, J., Del Pezzo, E., De Miguel, F., Herraiz, M., Alguacil, G., & Morales, J. (1990). Depth-dependent seismic attenuation in the Granada zone (Southern Spain). *Bulletin of the Seismological Society of America*, *80*(5), 1232–1244.

Jin, A., & Aki, K. (1988). Spatial and temporal correlation between coda Q and seismicity in China. *Bulletin of the Seismological Society of America*, *78*(2), 741–769.

Jin, A., & Aki, K. (2005). High-resolution maps of coda Q in Japan and their interpretation by the brittle-ductile interaction hypothesis, Earth. *Planets and Space*, *57*(5), 403–409.

Johnson, C. E. (1979). I. CEDAR—An Approach to the computer automation of short-period local seismic networks. II Seismotectonics of the Imperial Valley of Southern California (Ph.D. thesis), California Institute of Technology.

Kanamori, H. (1977). The energy release in great earthquakes. *Journal of Geophysical Research*, *82*(20), 2981–2987.

Kato, K., Aki, K., & Takemura, M. (1995). Site amplification from coda waves: Validation and application to S-wave site response. *Bulletin of the Seismological Society of America*, *85*(2), 467–477.

Koyanagi, S., Mayeda, K., & Aki, K. (1992). Frequency-dependent site amplification factors using the S-wave coda for the Island of Hawaii. *Bulletin of the Seismological Society of America*, *82*(3), 1151–1185.

Lee, W. H. K., Bennett, R., & Meagher, K. (1972). *A Method of Estimating Magnitude of Local Earthquakes from Signal Duration*. Geological Survey: US Department of the Interior.

Lin, Y.-P., & Jordan, T. H. (2018). Frequency-dependent attenuation of P and S waves in Southern California. *Journal of Geophysical Research: Solid Earth*, *123*, 5814–5830. https://doi.org/10.1029/2018JB015448

Madariaga, B. Y. R. (1976). Dynamics of an expanding circular fault. *Bulletin of the Seismological Society of America*, *66*(3), 639–666.

Madariaga, R. (2007). Seismic source theory. In H. Kanamori, & G. Schubert (Eds.), *Treatise on Geophysics* (vol. 59–82,. Amsterdam: Elsevier.

Margerin, L., Campillo, M., Shapiro, N., & van Tiggelen, B. (1999). Residence time of diffuse waves in the crust as a physical interpretation of coda Q: Application to seismograms recorded in Mexico. *Geophysical Journal International*, *138*(2), 343–352.

Margerin, L., Campillo, M., & Tiggelen, B. (1998). Radiative transfer and diffusion of waves in a layered medium: New insight into coda Q. *Geophysical Journal International*, *134*(2), 596–612.

Mayeda, K., Hofstetter, A., O'Boyle, J. L., & Walter, W. R. (2003). Stable and transportable regional magnitudes based on coda-derived moment-rate spectra. *Bulletin of the Seismological Society of America*, *93*(1), 224–239.

Mayeda, K., Koyanagi, S., & Aki, K. (1991). Site amplification from S-wave coda in the Long Valley Caldera region, California. *Bulletin of the Seismological Society of America*, *81*(6), 2194–2213.

Mayeda, K., Su, F., & Aki, K. (1991). Seismic albedo from the total seismic energy dependence on hypocentral distance in southern California. *Physics of the Earth and Planetary Interiors*, *67*(1-2), 104–114.

Mayeda, K., & Walter, W. R. (1996). Moment, energy, stress drop, and source spectra of western United States earthquakes from regional coda envelopes. *Journal of Geophysical Research*, *101*(B5), 11,195–11,208.

Menke, W. (2012). *Geophysical Data analysis: Discrete Inverse Theory: MATLAB Edition*, vol. 45. London: Academic Press.

Mitchell, B. J., Pan, Y., Xie, J., & Cong, L. (1997). Lg coda Q variation across Eurasia and its relation to crustal evolution. *Journal of Geophysical Research*, *102*(B10), 22,767–22,779.

Mukhopadhyay, S., Sharma, J., Massey, R., & Kayal, J. (2008). Lapse-time dependence of coda Q in the source region of the 1999 Chamoli earthquake. *Bulletin of the Seismological Society of America*, *98*(4), 2080–2086.

Oth, A., Bindi, D., Parolai, S., & Di Giacomo, D. (2011). Spectral analysis of k-NET and kik-NET data in Japan, part II: On attenuation characteristics, source spectra, and site response of borehole and surface stations. *Bulletin of the Seismological Society of America*, *101*(2), 667–687.

Paasschens, J. (1997). Solution of the time-dependent Boltzmann equation. *Physical Review E*, *56*(1), 1135.

Peng, J., Aki, K., Chouet, B., Johnson, P., Lee, W., Marks, S., et al. (1987). Temporal change in coda associated with the Round Valley, California, earthquake of November 23, 1984. *Journal of Geophysical Research*, *92*(B5), 3507–3526.

Phillips, W. S., & Aki, K. (1986). Site amplification of coda waves from local earthquakes in central California. *Bulletin of the Seismological Society of America*, *76*(3), 627–648.

Prieto, G. A., Shearer, P. M., Vernon, F. L., & Kilb, D. (2004). Earthquake source scaling and self-similarity estimation from stacking P and S spectra. *Journal of Geophysical Research*, *109*, B08310. https://doi.org/10.1029/2004JB003084

Pulli, J. J. (1984). Attenuation of coda waves in New England. *Bulletin of the Seismological Society of America*, *74*(4), 1149–1166.

Raoof, M., Herrmann, R., & Malagnini, L. (1999). Attenuation and excitation of three-component ground motion in southern California. *Bulletin of the Seismological Society of America*, *89*(4), 888–902.

Rautian, T., & Khalturin, V. (1978). The use of the coda for determination of the earthquake source spectrum. *Bulletin of the Seismological Society of America*, *68*(4), 923–948.

Roecker, S., Tucker, B., King, J., & Hatzfeld, D. (1982). Estimates of Q in central Asia as a function of frequency and depth using the coda of locally recorded earthquakes. *Bulletin of the Seismological Society of America*, *72*(1), 129–149.

Ross, Z. E., Ben-Zion, Y., White, M. C., & Vernon, F. L. (2016). Analysis of earthquake body wave spectra for potency and magnitude values: Implications for magnitude scaling relations. *Geophysical Journal International*, *207*(2), 1158–1164.
Sandwell, D. T., & Wessel, P. (2016). Interpolation of 2-D vector data using constraints from elasticity. *Geophysical Research Letters*, *43*, 10,703–10,709. https://doi.org/10.1002/2016GL070340
Sato, H., Fehler, M. C., & Maeda, T. (2012). *Seismic Wave Propagation and Scattering in the Heterogeneous Earth*, vol. 496. Heidelberg: Springer.
Sens-Schönfelder, C., & Wegler, U. (2006). Radiative transfer theory for estimation of the seismic moment. *Geophysical Journal International*, *167*(3), 1363–1372.
Shapiro, N., Campillo, M., Margerin, L., Singh, S., Kostoglodov, V., & Pacheco, J. (2000). The energy partitioning and the diffusive character of the seismic coda. *Bulletin of the Seismological Society of America*, *90*(3), 655–665.
Shearer, P. M. (2009). *Introduction to Seismology*. Cambridge: Cambridge University Press.
Shearer, P. M., Prieto, G. A., & Hauksson, E. (2006). Comprehensive analysis of earthquake source spectra in southern California. *Journal of Geophysical Research*, *111*, B06303. https://doi.org/10.1029/2005JB003979
Singh, S., & Herrmann, R. B. (1983). Regionalization of crustal coda Q in the continental United States. *Journal of Geophysical Research*, *88*(B1), 527–538.
Steck, L. K., Prothero, W. A., & Scheimer, J. (1989). Site-dependent coda Q at Mono Craters, California. *Bulletin of the Seismological Society of America*, *79*(5), 1559–1574.
Su, F., & Aki, K. (1990). Temporal and spatial variation on coda Q-1 associated with the North Palm Springs earthquake of July 8, 1986. *Pure and Applied Geophysics*, *133*, 23–52.
Su, F., & Aki, K. (1995). Site amplification factors in central and southern California determined from coda waves. *Bulletin of the Seismological Society of America*, *85*(2), 452–466.
Su, F., Aki, K., & Biswas, N. (1991). Discriminating quarry blasts from earthquakes using coda waves. *Bulletin of the Seismological Society of America*, *81*(1), 162–178.
Su, F., Aki, K., Teng, T., Zeng, Y., Koyanagi, S., & Mayeda, K. (1992). The relation between site amplification factor and surficial geology in central California. *Bulletin of the Seismological Society of America*, *82*(2), 580–602.
Sumiejski, L. E., & Shearer, P. M. (2012). Temporal stability of coda Q-1 in southern California. *Bulletin of the Seismological Society of America*, *102*(2), 873–877.
Suteau, A. M., & Whitcomb, J. H. (1979). A local earthquake coda magnitude and its relation to duration, moment Mo, and local Richter magnitude ML. *Bulletin of the Seismological Society of America*, *69*(2), 353–368.
Thatcher, W., & Hanks, T. C. (1973). Source parameters of southern California earthquakes. *Journal of Geophysical Research*, *78*(35), 8547–8576.
Trugman, D. T., & Shearer, P. M. (2017). Application of an improved spectral decomposition method to examine earthquake source scaling in southern California. *Journal of Geophysical Research: Solid Earth*, *122*, 2890–2910. https://doi.org/10.1002/2017JB013971
Tselentis, G.-A. (1997). Evidence for stability in coda Q associated with the Egion (central Greece) earthquake of 15 June 1995. *Bulletin of the Seismological Society of America*, *87*(6), 1679–1684.
Tsujiura, M. (1978). Spectral analysis of the coda waves from local earthquakes. *Bulletin of the Earthquake Research Institute*, *53*, 1–48.
Tsukuda, T. (1988). Coda-Q before and after the 1983 Misasa earthquake of M 6.2, Tottori Prefecture, Japan. *Pure and Applied Geophysics*, *128*(1), 261–279.
Tucker, B. E., & King, J. L. (1984). Dependence of sediment-filled valley response on the input amplitude and the valley properties. *Bulletin of the Seismological Society of America*, *74*, 153–165.
Wang, W., & Shearer, P. (2017). Using direct and coda wave envelopes to resolve the scattering and intrinsic attenuation structure of southern California. *Journal of Geophysical Research: Solid Earth*, *122*, 7236–7251. https://doi.org/10.1002/2016JB013810
Wang, J., Teng, T., & Ma, K. (1989). Temporal variation of coda-Q during Hualien earthquake of 1986 in eastern Taiwan. *Pure and Applied Geophysics*, *130*(4), 617–634.
Wegler, U. (2004). Diffusion of seismic waves in a thick layer: Theory and application to Vesuvius volcano. *Journal of Geophysical Research*, *109*, B07303. https://doi.org/10.1029/2004JB003048
Wennerberg, L. (1993). Multiple-scattering interpretations of coda-Q measurements. *Bulletin of the Seismological Society of America*, *83*(1), 279–290.
Woodgold, C. (1994). Coda Q in the Charlevoix, Quebec, region: Lapse-time dependence and spatial and temporal comparisons. *Bulletin of the Seismological Society of America*, *84*(4), 1123–1131.
Yang, W., Hauksson, E., & Shearer, P. M. (2012). Computing a large refined catalog of focal mechanisms for southern California (1981–2010): Temporal stability of the style of faulting. *Bulletin of the Seismological Society of America*, *102*(3), 1179–1194.
Yomogida, K., Aki, K., & Benites, R. (1997). Coda-Q in two-layer random media. *Geophysical Journal International*, *128*(2), 425–433.
Yoshimoto, K., & Jin, A. (2008). Coda energy distribution and attenuation. *Advances in Geophysics*, *50*, 265–299.
Yun, S., Lee, W. S., Lee, K., & Noh, M. H. (2007). Spatial distribution of coda Q in South Korea. *Bulletin of the Seismological Society of America*, *97*(3), 1012–1018.